J. Fluid Mech. (2000), *vol.* 410, *pp.* 67–99. Printed in the United Kingdom

A numerical study of three-dimensional orographic gravity-wave breaking observed in a hydraulic tank

By F. GHEUSI[1], J. STEIN[1] AND O. S. EIFF[1,2]

[1]Météo-France, Centre National de Recherches Météorologiques, 42 av. G.Coriolis, 31057 Toulouse Cedex, France

[2]Institut de Mécanique des Fluides de Toulouse, allée C.Soula, 31400 Toulouse, France

(Received 1 May 1998 and in revised form 16 December 1999)

Numerical simulations with a non-hydrostatic anelastic model are carried out to reproduce hydraulic tank experiments on stratified flow past a two-dimensional mountain ridge, for a Froude number of 0.6 and a Reynolds number of 200. The gravity wave thus generated steepens, overturns and breaks. Numerical simulations and experiments are directly compared showing close agreement. Ground friction is found to have a major influence. It induces a boundary-layer separation on the lee slope of the mountain and a low-level trapped lee wave inhibiting the downstream propagation of the breaking region above. Consequently, the three-dimensional vortices generated within the unstable two-dimensional overturning wave have a toroidal shape in agreement with experimental observations. Sensitivity to the shape of the initial three-dimensional perturbation is studied. In the case of harmonic disturbances, spectral analysis reveals that during the growth phase of the instability, harmonics are coherently produced by the nonlinear transverse advection term. During the later phase of quasi-steady turbulence, the vortices have a morphology that does not depend on the type of the initial perturbation.

1. Introduction

The flow of a stratified fluid over an obstacle generates internal gravity waves. Their theoretical understanding was initiated by Queney (1936, 1948), who derived analytical solutions from a linear model. For uniform upstream stratification and velocity, Long (1954) showed, using a nonlinear model, that the stationary isopycnals, obtained in the case of a sufficiently strong orographic perturbation, are overturned, leading to a region of static convective instability. However, Long's stationary solution is unstable. Indeed, any physical condition that leads the gravity wave to steepen and then overturn, eventually produces wave breaking. Orographic wave breaking has been studied, at the scale of the global flow, with numerical simulations (e.g. Clark & Peltier 1977, 1984; Scinocca & Peltier 1993, and many others) and laboratory experiments (e.g. Rottman & Smith 1989; Castro & Snyder 1993; Baines 1995, chap. 5).

These studies were mainly interested in the influence of the wave breaking on

surface wind and drag in the atmosphere, and its role in severe downslope windstorm events. However, they did not focus on the dynamics within the wave-breaking region itself. Even when generated over a two-dimensional topography, the gravity-wave breaking is a three-dimensional process, as first theoretically predicted by Klaasen & Peltier (1985) and explicitly simulated by Clark & Farley (1984). Strong internal waves induce intense shear in which three-dimensionalization processes may arise (Belcher & Hunt 1998) but the two-dimensional overturning of isopycnals in an initially stably stratified fluid also produces a region of static instability. Therefore, the three-dimensional instabilities in two-dimensional overturning waves were investigated more specifically. With a linear pertubation method, Klaasen & Peltier (1985, 1991) characterized the transverse unstable modes developing in a two-dimensional Kelvin–Helmholtz billow. This theoretical analysis was complemented with laboratory experiments by Thorpe (1985) and three-dimensional numerical simulations by Caulfield & Peltier (1994). Winters & D'Asaro (1994), Andreassen *et al.* (1994), Fritts, Isler & Andreassen (1994) and Dörnbrack (1998) numerically studied three-dimensional gravity-wave breaking induced by trapping the energy near a critical level in a shear layer. Afanasyev & Peltier (1998) investigated the breaking of an orographic gravity wave in a background flow with no underlying shear. All these studies revealed alternating vortices, oriented in the direction of the background flow (with different morphologies according to the breaking configuration). They all stressed the importance of buoyancy forces in the growth of the instability. Winters & Riley (1992) showed two mechanisms of instability, one dominated by shear for streamwise perturbations, and the other by convection for transverse perturbations. In the case of breaking near a critical layer, Fritts *et al.* (1994) note that the vortices are roughly circular in their early stage and that their horizontal and vertical scales are dictated by the depth of the convectively unstable region. This class of instabilities is invoked in scenarii of transition to turbulence within the breaking waves (Klaasen & Peltier 1985; Isler *et al.* 1994).

The present numerical study was carried out as a collaboration with an experimental counterpart (Eiff & Bonneton 1998, 2000), where the gravity-wave breaking is generated in a flow with uniform upstream velocity and stratification. This configuration is the same as in Long's model (Long 1954), and has been the object of most theoretical investigations. The physical conditions for our numerical simulations closely match the laboratory experiments, so that they can be compared directly. Good agreement via such direct comparisons provides immediate validation of the numerical model.

In § 2, we will describe the physical problem (§ 2.1), then the numerical set-up (§ 2.2). In § 3 we study the lee-wave dynamics in the longitudinal (x, z)-plane. Since the flow is perturbed by a two-dimensional obstacle, this study is first carried out with two-dimensional numerical simulations (§ 3.1). The simulation results are compared with the experimental results and orographic lee-wave theory (§ 3.2). In § 4 we focus on the flow within the breaking region, with the aid of three-dimensional simulations. In particular, we investigate the instability leading to three-dimensional motions from the two-dimensional overturning wave. The general evolution of the three-dimensional motions is presented in § 4.1. The geometry of the vortices at the end of the instability growth stage is depicted in § 4.2. Diagnostic tools such as autocorrelation functions and spectral scale analysis enable us to characteristize the vortices (§ 4.3). The instability is further analysed via experiments on the sensitivity to the type of the initial three-dimensional perturbation (§ 4.4). We conclude in § 5 with a discussion based on our numerical results.

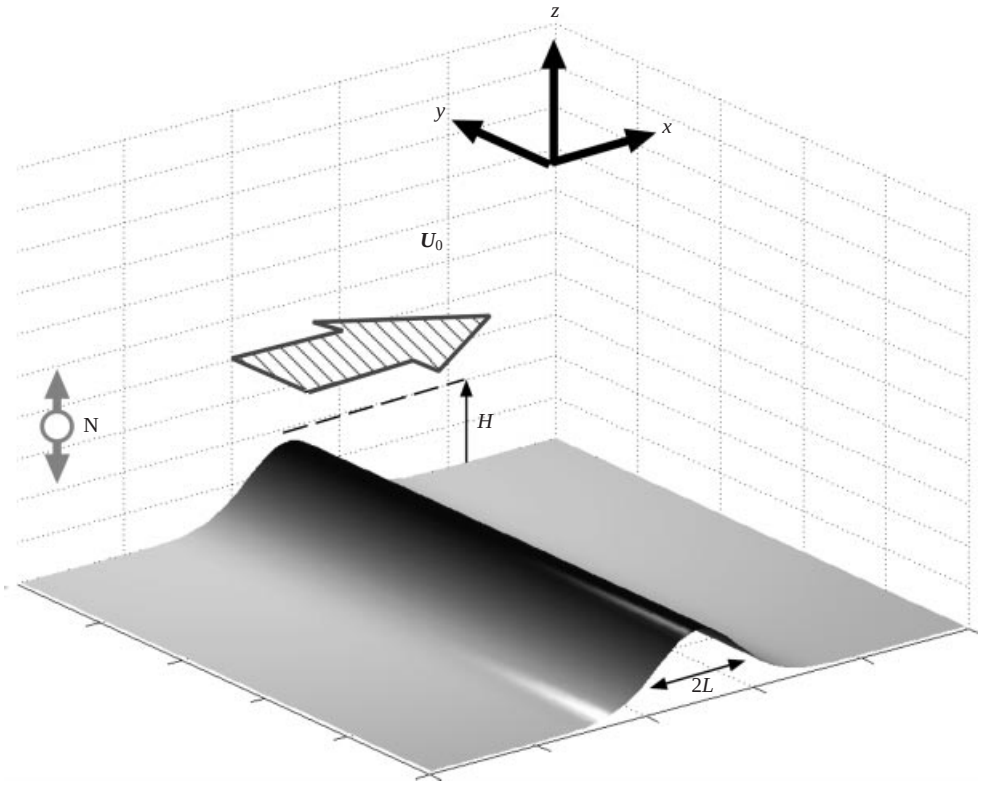

FIGURE 1. The physical problem.

2. Presentation of the study

2.1. *The physical problem*

In this paper, we study the fundamental problem of stratified flow over a two-dimensional mountain ridge (figure 1): the orography has a Gaussian shape of width L in the x-direction, and infinite extent in the y-direction, defined by $h(x, y) = He^{-(x/L)^2}$. The unperturbed flow is stably stratified by a vertical gradient of potential temperature, θ; the Brunt–Väisälä frequency is uniform, given by $N = (g/\Theta_{00}\, \mathrm{d}\theta_0/\mathrm{d}z)^{1/2} = 10^{-2}\,\mathrm{s}^{-1}$ (where $g = 9.81\,\mathrm{m\,s}^{-2}$, $\Theta_{00} = 285\,\mathrm{K}$ is a reference temperature), which is typical of tropospheric stability. Far upstream from the ridge, the vertical velocity profile is uniform and stationary: $\boldsymbol{u}_0(x = -\infty, y, z) = U_0\boldsymbol{e}_x$, where U_0 is set to $10\,\mathrm{m\,s}^{-1}$ ($\boldsymbol{e}_x$ is the unit vector along x).

The system is controlled by the following dimensionless numbers: the Reynolds number $Re = U_0H/\nu$ (where ν is the kinematic viscosity of the fluid); the Prandtl number $Pr = \nu/\kappa$, where κ is the appropriate diffusion coefficient†; the Froude number $F = U_0/NH$ which specifies the nonlinearity of the wave (nonlinear pertubations of the flow are obtained for a sufficiently high obstacle with respect to the vertical wavelength of the internal gravity waves $2\pi\, U_0/N$, hence for $F \lesssim 1$); the longitudinal Froude number $F_L = U_0/NL$ which is a measure of non-hydrostatic effects appearing for narrow obstacles (F_L is the ratio of $1/N$, the time of oscillation

† Molecular diffusion of salt in water (tank experiments), or thermal diffusion (the equivalent phenomenon for our numerical simulations).

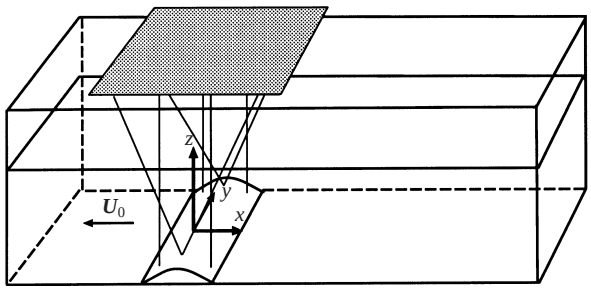

FIGURE 2. Experimental device used by Eiff & Bonneton (1998, 2000).

for a fluid parcel under buoyancy restoring forces, to L/U_0, the time of flow over the obstacle at speed U_0). See the reviews of Durran (1990) or Baines (1995) for more details about the theory of orographic internal gravity waves, and Bonneton, Auban & Perrier (1999) and Laprise & Peltier (1989) for a discussion of the influence of the Froude numbers.

The experimental procedure is briefly described here to introduce the conditions for the numerical simulations; for further details about these experiments and a detailed discussion of the experimental results, see Eiff & Bonneton (1998, 2000). The obstacle spans the whole width of the $0.5 \times 0.5 \times 4\ \mathrm{m}^3$ tank. It is towed just above the floor at constant velocity $\boldsymbol{U}_0$ in linearly salt-stratified water (figure 2). One must stress two important points resulting from the experimental procedure which must be taken into account in our numerical model: the existence of a small gap between the baseplate of the obstacle and the tank floor, and the quite unusual boundary conditions on the ground for a meteorological problem. In the obstacle frame, the channel floor is moving at speed $\boldsymbol{U}_0$, so that the condition of fluid adherence is $\boldsymbol{u} = 0$ on the obstacle surface, but $\boldsymbol{u} = \boldsymbol{U}_0$ on the ground far from the obstacle.

The dimensionless parameters governing the experimental conditions are $Re \sim 200$, $Pr = 675$, $F = 0.6$, $F_L = 0.24$ (i.e. $L/H = 2.5$). The width of the channel, W/H, is 23.1 and the depth of the stratified water, D/H, about 9. The Froude number, F, corresponds to a highly nonlinear situation for which the gravity wave generated by the obstacle on the lee side gradually steepens and eventually breaks. The longitudinal Froude number, F_L, being smaller than 1, implies a non-hydrostatic regime. Since $Pr \gg 1$, salt (or thermal) diffusion will be negligible with respect to viscous momentum diffusion.

2.2. *Numerical methodology*

2.2.1. *The numerical model*

The *Meso-NH* atmospheric non-hydrostatic meso-scale simulation system (Lafore *et al.* 1997), jointly developed by the Laboratoire d'Aérologie (Toulouse, France) and the CNRM (Météo-France), enables the simulation of atmospheric motions, ranging from the synoptic scale (a few thousands of kilometres) to the large turbulent eddy scale (a few tenths of metres). The model is based on the Lipps & Helmer (1982) modified anelastic system of equations (in order to filter acoustic waves, which are not of interest in meteorology). In this study, it is used with Boussinesq's hypothesis (Scinocca & Shepherd 1992), in order to take into account the incompressibility of salted water in the experiments. We also neglect the Earth's sphericity and rotation (which are usually taken into account in the complete *Meso-NH* model).

Under these hypotheses, the equations are

$$\rho' = -\rho_0 \left(\frac{\theta'}{\Theta_{00}} \right), \tag{2.1}$$

$$\nabla \cdot \boldsymbol{u} = 0, \tag{2.2}$$

$$\frac{\partial}{\partial t}(\rho_0 \boldsymbol{u}) + \nabla \cdot (\rho_0 \boldsymbol{u} \otimes \boldsymbol{u}) + C_p \Theta_{00} \rho_0 \nabla \Pi' + \rho_0 \boldsymbol{g} \frac{\theta - \Theta_{00}}{\Theta_{00}} - \mathscr{F}_{\boldsymbol{m}} = 0, \tag{2.3}$$

$$\frac{\partial}{\partial t}(\rho_0 \theta) + \nabla \cdot (\rho_0 \theta \, \boldsymbol{u}) - \mathscr{F}_t = 0. \tag{2.4}$$

The thermodynamical fields have been written as

$$\theta(x, y, z, t) = \Theta_{00} + \theta'(x, y, z, t), \tag{2.5}$$

$$\Pi(x, y, z, t) = \Pi_0(z) + \Pi'(x, y, z, t). \tag{2.6}$$

The subscript 0 refers to the background field and the prime to the perturbation. $\Pi = \left(p/p_{00}\right)^{(R/C_p)}$ is Exner's function and $p_{00} = 10^5$ Pa the reference pressure. $\Theta_{00} = 285$ K is the (constant) reference temperature. The background state is in hydrostatic equilibrium:

$$\Pi_0(z) = -\frac{gz}{C_p \Theta_{00}}.$$

Equation (2.1) is the linearized equation of state, (2.2) the continuity equation, (2.3) the momentum equation and (2.4) the thermodynamic equation. $\mathscr{F}_{\boldsymbol{m}} = \nabla \cdot [\nu \rho_0 \nabla(\boldsymbol{u})]$ and $\mathscr{F}_t = \nabla \cdot \left[(\nu/Pr)\rho_0 \nabla(\theta)\right]$ represent the influence of momentum and thermal diffusivity, respectively.

The orography is included by the use of the Gal-Chen & Sommerville (1975) terrain-following coordinate in the model computation:

$$\overline{z} = H \frac{z - h(x)}{H - h(x)}.$$

The model discretization is in the spirit of Clark (1977). The spatial discretization is based on second-order-accurate centred finite differences on an Arakawa C grid (Arakawa & Mesinger 1976). The flux form of equations (3) and (4) is preserved by using at the same time the covariant and contravariant components of the velocity (Viviand 1974). The temporal discretization is purely explicit, and a weak time filter (Asselin 1972) is applied to control the rapid oscillations generated by the leapfrog treatment of the equations. The incompressible form of the continuity equation (2.2) is a strong constraint which is enforced by solving an elliptic equation for the pressure at every time step. Its resolution in terrain-following coordinates is based on a 'flat' operator (i.e. the operator obtained by removing the orography) inverted by a FFT algorithm for the horizontal part and a tri-diagonal algorithm for the vertical part. The 'flat' operator is used to precondition the problem with orography, which is solved with a Richardson's iterative algorithm. The complete description of the *Meso-NH* numerical discretization and schemes can be found in Lafore *et al.* (1997).

2.2.2. *Physical parameters, boundary conditions and grid*

A summary of all the numerical simulations considered in this paper is given in table 1. The physical parameters are chosen to be in accordance with the dimensionless numbers of the hydraulic experiments, given in § 2.1 (i.e. $Re = 200$, $Pr = 675$,

Mountain height	$H = 1667\,\mathrm{m}$
Mountain width	$L = 4167\,\mathrm{m}$
Stratification	$N = 0.01\,\mathrm{s}^{-1}$
Basic velocity	$U_0 = 10\,\mathrm{m\,s}^{-1}$
Viscosity	$\nu = 82.5\,\mathrm{m}^2\,\mathrm{s}^{-1}$
Boundary conditions:	
$x = -12L, +20L$	radiative
$z = 9H$ (top)	rigid, free slip
$z = h(x)$ (ground)	rigid, viscous layer (sim. 1 to 9), free slip (sim. 1b)

Simulation	1, 1b	2	3	4	5	6, 7, 8	9
Domain along x	whole	sub[(a)]	sub	sub	sub	sub	sub
Domain width, L_y	—	$4H$	$4H$	$32H$	$32H$	$4H$	$23H$
B.C. at $y = 0$, L_y	—	cyclic	cyclic	cyclic	cyclic	cyclic	wall
Number of points in x	320	128	256	128	64	128	90
Number of points in y	1 (2-D)	32	64	256	128	32	128
Number of points in z				56			
Δx	$L/10$	$L/20$	$L/40$	$L/20$	$L/10$	$L/20$	$L/14$
Δy	—	$L/20$	$L/40$	$L/20$	$L/10$	$L/20$	$L/14$
Δz				$0.25\,U_0/N \simeq L/17$			
$N\Delta t$	0.03	0.02	0.01	0.02	0.04	0.02	0.02
3-D disturbance	—	white[(b)]	white	white	$n = 2$[(c)]	$n = 1, 2, 4$[(c)]	none

TABLE 1. Details of the numerical simulations presented in this paper. (*a*) sub: only the subdomain is simulated (with a finer interpolated grid, as shown in figure 3 and explained in § 2.2.2). (*b*) white: the flow is perturbed with a three-dimensional white noise. (*c*) $n = ..$: the disturbance on θ is harmonic along the y-direction with wavelength $\lambda = L_y/n$.

$F = 0.6$, $F_L = 0.24$, $W/H = 23.1$, $D/H = 9$). However, they are adjusted with the meteorologically meaningful values of $U_0 = 10$ m s^{-1} and $N = 0.01$ s^{-1}, leading to $H = 1667$ m but also to an artificially high viscosity of $\nu = 82.5$ m^2 s^{-1}.

The transverse width of the simulation domain, L_y, is not necessarily chosen to be similar to the tank width. In order to simulate the wave breaking over two-dimensional orography with implied infinite extent, cyclic lateral boundary conditions are used. There is hence no explicit need to be geometrically similar with the experimental configuration, and the width chosen is either $L_y = 4H$ or $32H$. However, the sidewalls of the channel are directly taken into account in simulation 9, and in this case the width of the domain is $23H$ as in the hydraulic tank, while the lateral boundary conditions simulate rigid walls with viscous friction.

The height of the simulated domain is equal to the depth of the stratified water in the channel. The upper boundary condition is modelled with a rigid roof and a free-slip condition. Hence, the gravity waves in the numerical model are reflected at the upper boundary in an approximately similar way to the free surface of the tank experiments. However, the experimental study by Eiff & Bonneton (1998) and some numerical sensitivity tests have shown that in the breaking-wave case studied here, the upper boundary condition significantly influences the wave dynamics only at levels largely above the wave-breaking region.

The boundary conditions at the extremities in x are wave-radiative open. Following Davies (1976) and Carpenter (1982), the normal velocity u is given by a Sommerfeld condition, but we add to the radiative equation a Rayleigh term which relaxes the field towards its large-scale value (subscripted by LS):

$$\frac{\partial}{\partial t}(u - u_{LS}) = -(u + c)\frac{\partial}{\partial x}(u - u_{LS}) - \frac{u - u_{LS}}{\tau}.$$

The large-scale value is set to the reference background state value, $U_0 \boldsymbol{e}_x$, for the large domain simulation 1 (see table 1), or to the output value of the coupling large-scale model for the nested simulations 2 to 9. c is a phase velocity set to 20 m s^{-1} and τ is a characteristic time for the relaxation. We choose $\tau = 4\Delta t$. The other prognostic variables at the boundaries are either set to their large-scale values for incoming flow, or extrapolated from the model interior for outgoing flow.

The viscous $z = 0$ boundary condition is not explicitly expressed through adherence to the ground, since the first horizontal-velocity level in the simulation grid is located at $z = \Delta z/2$ (where Δz is the vertical size of the grid mesh). Rather, it is expressed with a forced vertical flux of horizontal momentum at $z = 0$. That flux is calculated on two assumptions: adherence to the ground and a linear† profile of horizontal velocity from $z = 0$ to $z = \Delta z/2$. The expression for the adherence condition depends on the location (remember that $\boldsymbol{u} = 0$ at the obstacle surface but $\boldsymbol{u} = U_0 \boldsymbol{e}_x$ far from the obstacle), as well as the gap, $\delta \simeq 0.8\,\Delta z/2$, between the obstacle and the bottom of the channel. The surface vertical flux of x-momentum, for example, is given by

$$\sigma_{xz}(z = h(x)) = \rho\nu \frac{u(z = \Delta z/2) - 0}{\Delta z/2} \quad \text{for } -1.75L < x < +1.75L,$$

$$\sigma_{xz}(z = h(x)) = \rho\nu \frac{u(z = \Delta z/2) - U_0}{\Delta z/2 + \delta} \quad \text{for } |x| > 1.75L$$

($x = 0$ corresponds to the mountain crest).

In general, the fluid at the ground will be much more strongly decelerated near the obstacle than far from it. For example, the ratio of the ground momentum fluxes near/far from the mountain is about 4 for $u(z = \Delta z/2) = 2U_0$. In simulation 9, the viscous adherence at $y = 0$ or $y = L_y$ on the sidewalls is taken into account in the same way. The implementation of the viscous boundary condition has been validated with a simulation of the analytically solvable problem of a viscous flow along a infinite plane plate. The mean relative deviation never exceeded 0.02%.

The initialization proceeds as follows. The fluid is initially at rest, in hydrostatic equilibrium with uniform stability N. It is accelerated by adding a uniform and stationary pressure gradient oriented towards positive x, so that the fluid velocity far upstream reaches $U_0 \boldsymbol{e}_x$ after $3.2N^{-1}$. Then, that gradient is no longer applied. This instant is chosen as time origin $t = 0$.

The model was previously validated for the case of non-breaking orographic gravity waves by Lafore *et al.* (1997). Such simulations only require a rather coarse grid $\Delta x = \Delta y = L/5$ in the horizontal (Stein 1992), with a vertical resolution

† According to experimental results for the boundary layer along a smooth wall (Schlichting 1979, chap. XX), the friction regime is purely laminar at the altitude $z = \Delta z/2$ for values of $(u^* \Delta z/2)/\nu$ up to 5 (where $u^* = [\nu u_\parallel/(\Delta z/2)]^{1/2}$ is the friction velocity and $u_\parallel = u_\parallel(z = \Delta z/2)$ is the velocity component parallel to the boundary). The friction is both laminar and turbulent for values between 5 and 70, and purely turbulent (logarithmic profile) above 70. Since $u_\parallel$ is lower than or of the order of $2U_0$, $(u^* \Delta z/2)/\nu$ remains lower than 6. The hypothesis of linear velocity profile up to $z = \Delta z/2$ thus appears to be satisfactory.

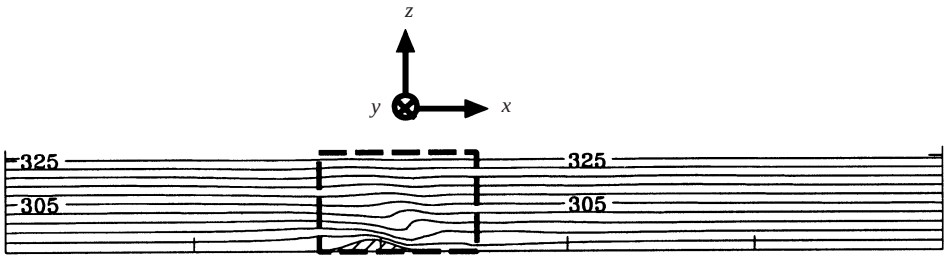

FIGURE 3. Full simulation domain, where iso-θ lines are plotted at $t = 15N^{-1}$ (θ in K). The dashed box delimits the nested fine grid subdomain for the three-dimensional simulations (2 to 9).

$\Delta z = 0.25U_0/N$. In the case of wave breaking, however, the breaking leads to a turbulent zone where the scales of the flow are smaller than in the wave field. Yet, due to the small value of the Reynolds number in our simulations ($Re = 200$), the conditions for direct numerical simulation can be approached with a reasonably fine grid. Although Kolmogorov's theory is strictly valid only for high Reynolds numbers, it allows us to estimate the size of the smallest eddies, which is of the same order of magnitude as the dissipation scale: Re can be related to the dissipation scale λ_d and the scale of energetic supply λ_e via $Re = (\lambda_e/\lambda_d)^{4/3}$ (e.g. Landau & Lifschitz 1959). With $Re = 200$ and $\lambda_e = H$, the condition for direct simulations, $\Delta x < \lambda_d$, requires $\Delta x < H/50$, or equivalently $\Delta x < L/125$.

The simulations presented in this study use $\Delta x = \Delta y = L/10$, $L/20$ or $L/40$ as mesh sizes. It implies that the very smallest eddies may be not resolved by the model. However, since the processes of the breaking dynamics of interest in our study occur at scales much larger than these eddies, no parametrization of the subgrid dynamics is used. The validity of such simulations will be discussed in § 4.3.

Along the x-direction, the domain extends $12L$ upstream of the mountain crest ($x = 0$) and $20L$ downstream. Unlike the two-dimensional simulations 1 and 1b, which are performed in this full domain, the three-dimensional simulations (2 to 9) need to be performed in a domain truncated in x with a model-nesting method, in order to reduce numerical costs. We adopt the following one-way nesting procedure. While $t < 15N^{-1}$, the gravity wave is not yet breaking and is therefore sufficiently captured with a coarse mesh ($\Delta x = \Delta y = L/5$). At $t = 15N^{-1}$, a portion of the coarse model (hereafter the subdomain) is interpolated into a finer grid (with various ratios depending on the simulation). The interpolated subdomain includes the full height and width of the large domain, but is limited at $x = -2.4L$ and $x = +3.8L$ (see figure 3), in order to contain the whole breaking wave at all times. For $t > 15N^{-1}$, the output of the coarse model (in the full domain) provides the time-dependent x-boundary conditions for the fine-mesh model (in the subdomain).

3. The gravity wave field

In this section, the experimental results in the longitudinal (x, z)-vertical plane will be compared to those of a two-dimensional simulation (simulation 1, see table 1).

3.1. *Two-dimensional simulations*

In the early stages of evolution, the propagation of the orographic gravity wave leads to a progressive steepening of the iso-θ contours at altitude $\simeq 2H$ and $\simeq 3H$ downstream from the crest (figure 4). They overturn around $t = 20N^{-1}$, leading to

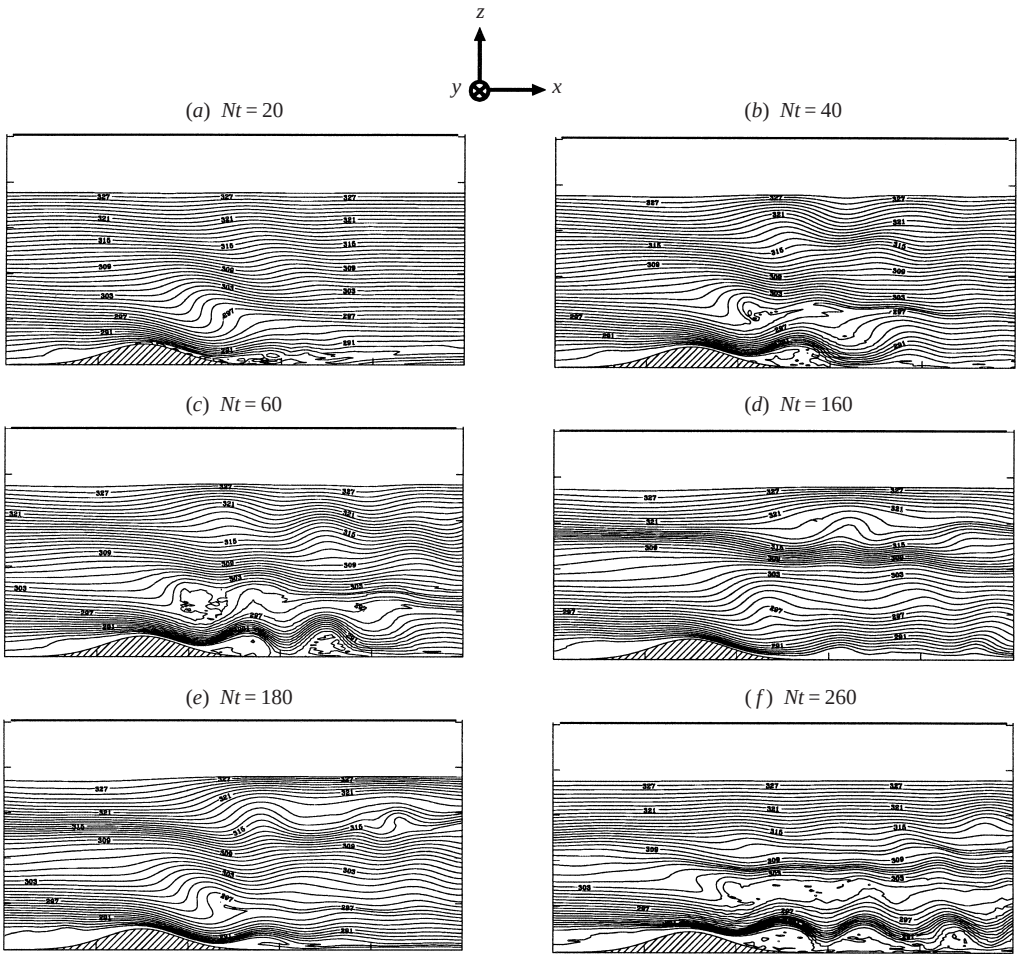

FIGURE 4. Time evolution of iso-θ (in K) contours. Simulation 1.

a convectively unstable region. The wave breaks during a span of about $20N^{-1}$ to form a mixed region of depth $\simeq 1.6H$. The evolution of this breaking zone continues to be non-stationary. For example, at $t = 160N^{-1}$ the flow is again laminar, and the wave starts steepening again and breaks anew around $t = 180N^{-1}$. The time scale of this evolution is rather long, of the order of $100N^{-1}$. However, these intermittent phenomena have to be considered cautiously, since they are likely due to the two-dimensional symmetry of this simulation. This point is discussed in § 5.

The propagation of the gravity waves produces a secondary wave above the primary breaking wave, steepening between altitudes of about $6H$ and $7H$. This steepening appears with a slight delay with respect to the primary wave, but the secondary wave never breaks. The steepening seems to be correlated with the activity of the main wave (compare, for example, $t = 60N^{-1}$ vs. $t = 160N^{-1}$ in figure 4): the larger the mixed zone of the lower wave, the weaker the steepening of the secondary wave.

In the lowest levels, the fluid is strongly accelerated, up to a maximum velocity of around $3\,U_0$. Further downstream, up to three oscillations of a non-hydrostatic trapped lee wave are visible near the ground in figure 4. It must be stressed that no linear trapped lee wave can be generated in the underlying reference flow, since the

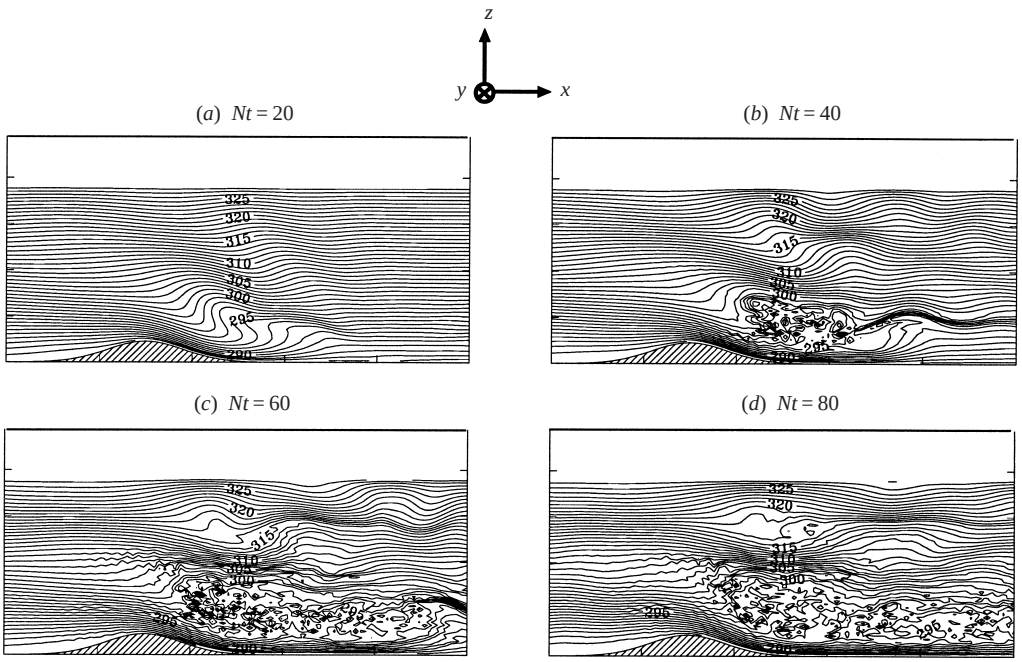

FIGURE 5. Time evolution of iso-θ (in K) contours. Simulation 1b.

background stability is uniform with no shear. Actually, the oscillations appear as soon as the breaking occurs, and are correlated in number and amplitude with the streamwise extent of the overlaying mixed region created by the wave breaking. For example, at $t = 160N^{-1}$, neither a mixed region nor a lee wave are observed, while at $t = 260N^{-1}$, both are well developed. Hence the trapped lee wave appears to be directly related to the nonlinear wave-breaking, by trapping its energy between the mixed region and the ground. Figure 4 also reveals that the first oscillation consists of a separation of the laminar boundary layer on the lee slope of the mountain. In order to study the link between the separation and the trapped lee wave, we performed a two-dimensional simulation (simulation 1b), which matches simulation 1, except for using a free-slip condition instead of friction at the ground. The flow field evolution is shown in figure 5. The geometry of the breaking wave in the longitudinal plane is considerably modified compared to the case with ground friction. The overturning of isopycnals occurs earlier and at lower altitude (i.e. for lower values of θ), as revealed by comparing simulation 1 and 1b at $t = 20N^{-1}$ (figures 4*a* and 5*a*). Indeed, the absence of friction enhances the downslope acceleration of the flow (with a maximum velocity of about $3.5\,U_0$) as well as the downstream advection of fluid in the bottom portion of the overturning region. Furthermore, the mixed region resulting from the wave breaking continuously extends further downstream. Both the mixed region and the associated lower layer of accelerated fluid propagate at a velocity of about $U_0/3$. This propagation occurring only under a free-slip condition at the ground is in agreement with Richard, Mascart & Nickerson (1989). Moreover, no trapped lee wave can be observed. We conclude that the boundary-layer separation on the lee slope of the mountain is dynamically controlled, specifically by ground friction. The presence of the mixed region above enables the trapping of a lee wave, which is likely to be excited by the boundary-layer separation. In return, the trapped lee wave

	Experiment	Simulation 1	Theory
Height of the (unperturbed) critical streamline, H_d	3.2	3.0	3.2
Depth of the blocked layer, b	0.37	0.33	0.40
Height of the mixed layer bottom, H_t	1.8	1.8	?
Depth of the mixed layer, D_{ml}	1.7	1.6	?
Horizontal distance of the critical point from the crest, x_c	1.5	1.7	?
Distance of the critical point C from the point O (see figure 6a), OC	2.6	2.5	2.8
Wavelength of the trapped lee waves, λ_{tlw}	4.6	4.7	~ 4

TABLE 2. Quantitative comparison of experimental, numerical and theoretical flow dimensions at $t = 50N^{-1}$. All data are expressed in units of H.

greatly influences the evolution and geometry of the mixed region above. It inhibits the continuous streamwise propagation of the mixed region, which instead consists of cores of mixed (or slightly stable) fluid above the troughs of the trapped lee wave (e.g. figures 4c or 4f). This point marks an important difference with the case of wave breaking studied by Afanasyev & Peltier (1998) who considered a free-slip condition on the ground.

The two interactions described above (i.e. the interaction of the mixed region with both the trapped lee waves and the upper secondary wave) are in accord with the theory (Peltier & Clark 1979, 1983; Clark & Peltier 1984) that the breaking region acts as a reflector which inhibits the upwards transmission of the energy of the orographic perturbation and traps it below (at least for the range of scales corresponding to the trapped lee wave).

It should also be observed that a stagnation region upstream of the mountain is present at the ground. Its depth, as judged by the first iso-θ contour, is evaluated as about $H/3$ (but with a large uncertainty since $\Delta z \simeq H/7$).

3.2. *Comparison with experiments*

The experimental results consisting of particle pathline visualizations are compared to the simulated iso-θ contours (simulation 1). Since thermal diffusion is negligible ($Pr = \nu/\kappa = 675$), the flow is adiabatic, hence θ is a Lagrangian invariant and iso-θ contours are consequently equivalent to streaklines (which are lines which would be traced out by a neutrally buoyant marker fluid continuously injected into the flow field at a fixed point in space). Strictly, streaklines and pathlines are identical only for stationary flows. However, this property remains approximately true for weak non-stationarity. In the laminar region outside the wave breaking, the flow does not significantly evolve during the integration time, $5N^{-1}$ to $10N^{-1}$, of the particle paths. Hence, the coincidence between pathlines and streaklines is good, and both can also be considered as streamlines.

For a detailed comparison, we choose to examine the wave field at $t = 50N^{-1}$, after the wave has broken. Figures 6(a) and 6(b) show the respective numerical and experimental results in the vertical (x, z)-plane. Table 2 gives a summary of the deduced flow dimensions as defined in figure 6(a), as well as theoretical values when available. Smith (1985) suggests a sketch of the wave-breaking configuration, wherein a critical streamline divides and encompasses a region of uniform density (the wave-breaking region). Smith (1989) gives the height H_d of this critical streamline in an hydrostatic

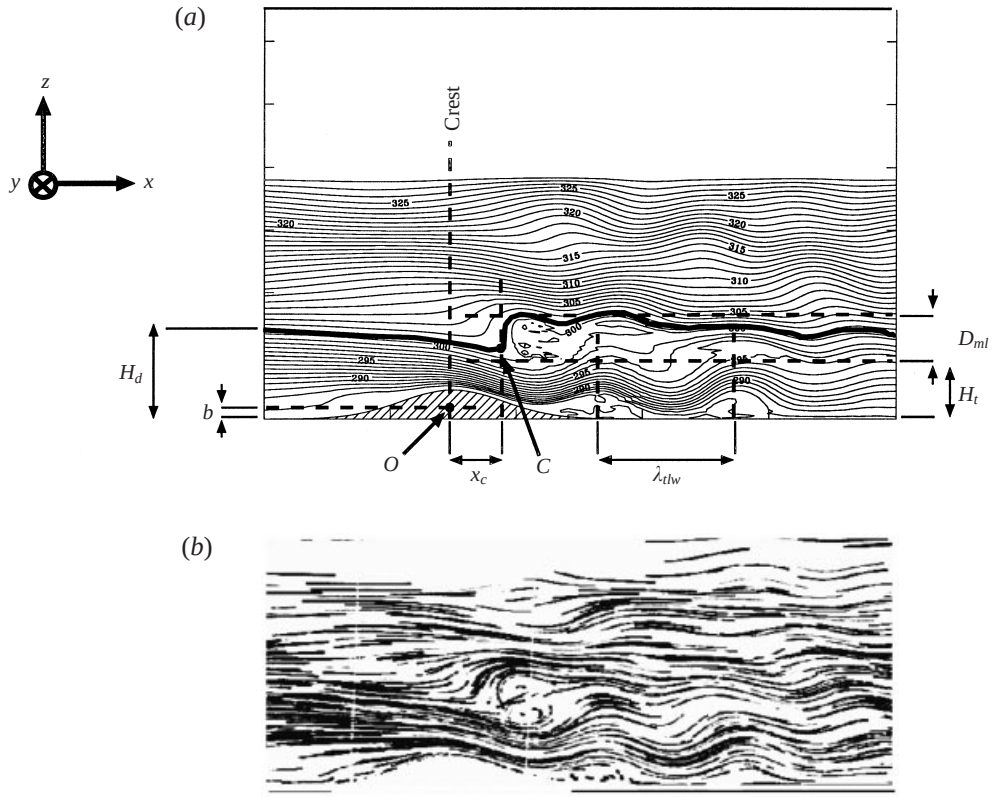

FIGURE 6. Vertical-plane results at $t = 50N^{-1}$. (*a*) Iso-θ (in K) contours. Simulation 1. (*b*) Pathlines in the hydraulic tank experiment (integration time $= 5N^{-1}$).

flow as $H_d = \frac{3}{4}\lambda + b$, where $\lambda = 2\pi U_0/N$ and $b = H - 0.985\,U_0/N \simeq H - U_0/N$ is the depth of the blocked layer. The theoretical values of H_d and b in table 2 are calculated according to these formulae, and the theoretical value for OC is taken as $\frac{3}{4}\lambda$, following Peltier & Clark (1979) and Smith (1989). It is more difficult to evaluate the experimental value of b from figure 6(*b*). Instead, a pseudo-experimental value, taken as the difference $H_{d\,exp} - \frac{3}{4}\lambda$, is used. A theoretical value for the wavelength of the trapped lee wave, λ_{tlw}, is also difficult to obtain since the trapped lee wave is due to the nonlinear orographic perturbation of the flow, especially under conditions of wave breaking, as discussed in § 3.1. The two-layer theory of Scorer (1949) requires two Brunt–Väisälä frequencies, one for the lower layer (trapped-lee-wave region) and one for the upper layer (the breaking region). Since the choice of these two frequencies would be meaningless in our case, we instead choose to estimate λ_{tlw} by an order-of-magnitude analysis. Taking $2\pi U_0/NH$, the distance over which an air parcel is flowing at speed U_0 and oscillating vertically at frequency $N/2\pi$, we obtain a value of $\lambda_{tlw} \sim 4H$.

The values cited in table 2 suggest a very good overall agreement between the simulation and the experiment, as well as the theory (when available). The general agreement is within 10%, well within the uncertainties of evaluation. The good agreement for the values H_d, x_c and OC is not surprising, because these dimensions are controlled by the wave dynamics, which are well captured even with a coarser grid (as discussed in § 2.2.2). The agreement for the values of H_t, D_{ml}, and λ_{tlw} demonstrates

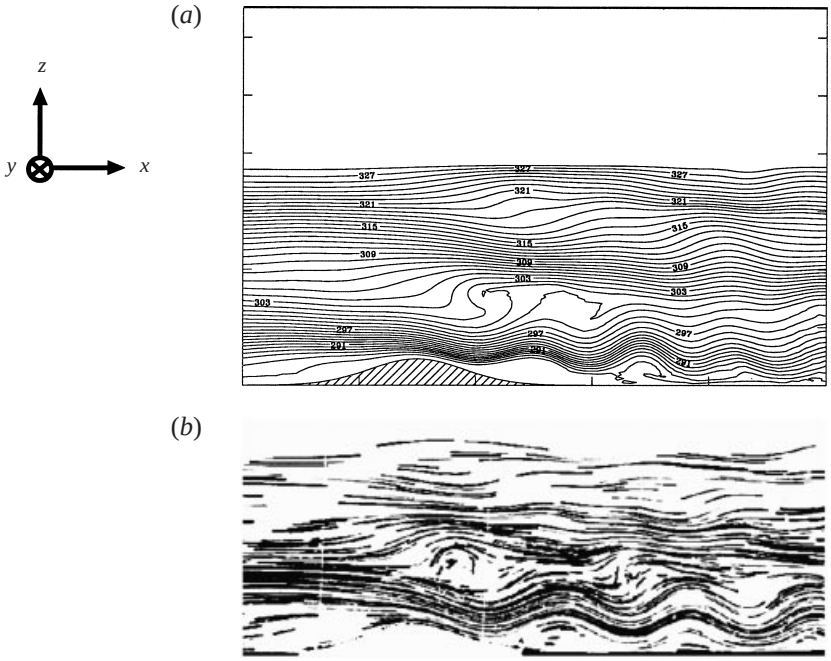

FIGURE 7. As figure 6 but at $t = 100N^{-1}$.

that the simulation captures the nonlinear effects of the flow quite satisfactorily. It should be noted that although Smith's theory yielding H_d and OC assumes the flow to be hydrostatic, the results appear to be at least extendable to the non-hydrostatic case studied here ($F_L = 0.24$).

The temporal evolution of the flow observed in the experiment and the simulation is also found to be comparable. In both cases, the wave steepens until about $t = 20N^{-1}$ and the breaking region is well mixed by $t = 50N^{-1}$. Comparison at later times (for example at $t = 100N^{-1}$, figure 7) confirms the presence of a secondary downstream core of mixing in the trough between the first two oscillations of the trapped lee wave, as discussed in § 3.1.

4. The dynamics within the wave-breaking region

The overturning wave induced by the two-dimensional topography produces instablity with respect to three-dimensional disturbances, as first predicted by the theory of Klaasen & Peltier (1985), and numerically simulated by Clark & Farley (1984). Counter-rotating pairs of vortices oriented in the streamwise direction are encountered in overturning internal waves in general (Caulfield & Peltier 1994; Fritts *et al.* 1994; Dörnbrack 1998; Afanasyev & Peltier 1998). Fritts *et al.* (1994) note that both the vertical and transverse scales of the vortices are close to the depth of the statically unstable layer. The hydraulic experiments by Eiff & Bonneton (2000) show that three-dimensional vortices emerge in the wave-breaking region. They appear as counter-rotating vortex pairs in the (x, y)-, (x, z)- and (y, z)-planes, and each vortex has a diameter of about $1.5H$, i.e. approximately equal to the depth of the breaking layer (see figure 8, for example in the (x, y)-plane). Further observations lead Eiff &

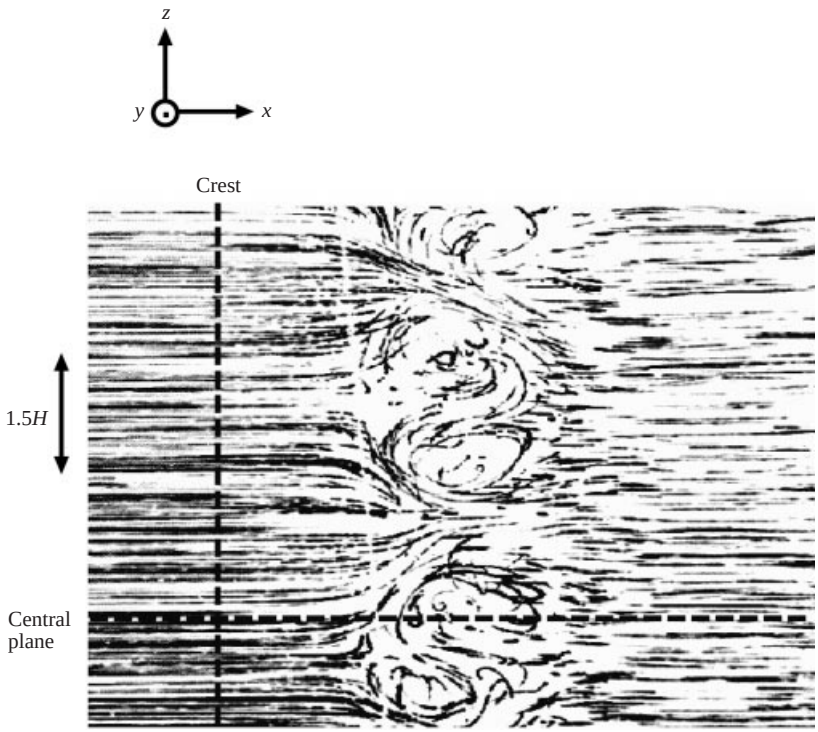

FIGURE 8. Experimental pathlines (integration time $= 10N^{-1}$) at $t = 50N^{-1}$ in the horizontal plane $z = 3H$, intersecting the breaking region.

Bonneton (2000) to suggest that these vortices, seen as counter-rotative in a given plane, actually are part of a toroidal structure (in terms of vorticity lines).

In order to study these three-dimensional motions, the two-dimensional symmetry needs to be broken in the numerical model with a three-dimensional disturbance. We choose to perturb θ at the level $\bar{z} = 2.3H$ which crosses the breaking region. The disturbance ϑ' which is added to θ will either be a (spatial) white noise, where all scales are equally excited, or harmonic along the y-direction, as defined by $\vartheta' = \vartheta_0 \sin(2\pi ny/L_y)$, where n is the wavenumber, $\vartheta_0 = 0.3\,\mathrm{K}$, and $L_y = N_y \Delta y$ is the width of the model domain. The disturbance is added at $t = 15N^{-1}$ to θ in the nested fine mesh model just before its implementation (see § 2.2.2 for the description of the nesting procedure).

4.1. *General evolution of the three-dimensional motions*

Let us define $\boldsymbol{u}'_{3D}(x, y, z, t)$ as the deviation from two-dimensionality for the velocity vector: $\boldsymbol{u}'_{3D}(x, y, z, t) = \boldsymbol{u}(x, y, z, t) - \langle \boldsymbol{u} \rangle_{L_y}(x, z, t)$ (where $\langle \boldsymbol{u} \rangle_{L_y}(x, z, t) = (1/L_y) \int_0^{L_y} \boldsymbol{u}(x, y, z, t)\,\mathrm{d}y$ is the mean value of $\boldsymbol{u}$ over the width L_y of the domain). A sample $\boldsymbol{u}'_{3D}$ field (figure 9) shows that the flow is significantly three-dimensional only within the breaking region and under the first crest of the trapped lee wave, that is in regions where the stratification is unstable or weak. Outside of these regions, the dynamics are quasi-two-dimensional and remain very similar to the two-dimensional simulation.

In order to characterize the three-dimensional instability of the wave breaking process, we evaluate the contribution of each component of $\boldsymbol{u}'_{3D}$ to the mean kinetic

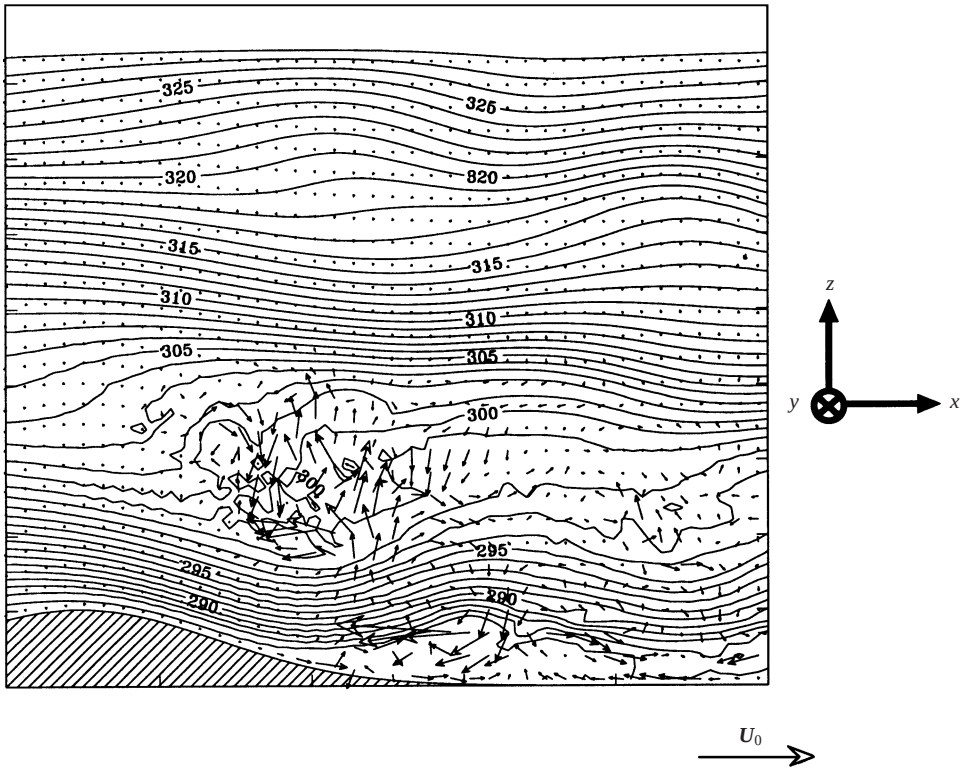

FIGURE 9. Iso-θ (in K) contours and $\boldsymbol{u}'_{3D}$ vector field in an (x,z)-plane at $t = 55N^{-1}$. Simulation 4.

energy of the three-dimensional motions, i.e. $\langle u'^2_{3D}\rangle$, $\langle v'^2_{3D}\rangle$ and $\langle w'^2_{3D}\rangle$. These mean values are calculated over 1280 points located within the breaking region.

The evolution of $\langle u'^2_{3D}\rangle$ and $\langle v'^2_{3D}\rangle$ (figure 10) reveals three distinct stages. After the introduction of the disturbance (at $t = 15N^{-1}$), $\langle u'^2_{3D}\rangle$ and $\langle v'^2_{3D}\rangle$ decay until $t \simeq 20N^{-1}$. For $t > 20N^{-1}$, $\langle u'^2_{3D}\rangle$ and $\langle v'^2_{3D}\rangle$ grow exponentially such that $(\langle u'^2_{3D}\rangle)^{1/2}$, $(\langle v'^2_{3D}\rangle)^{1/2} \sim \mathrm{e}^{+Nt/5}$, and finally reach saturation at $t \simeq 40N^{-1}$, with u'_{3D}, $v'_{3D} \sim 2$ m s^{-1}. Thereafter, the flow is sustained in a quasi-steady regime. From an inspection of the flow, it can be inferred that the three-dimensional instability starts developing as soon as the steepest iso-θ are vertical, that is as soon as the thermal profile becomes convectively unstable. Dörnbrack (1998) was led to similar conclusions in the case of a shear-stratified flow beneath a critical level. He evaluated the growth time to be about $3N^{-1}$ (compared to $5N^{-1}$ in our case), but noted that the growth time increases with decreasing Reynolds number, which may explain the slightly slower growth in our simulation. Hereafter, we will respectively refer to these two stages of the evolution as the *growth regime* ($20N^{-1} < t < 40N^{-1}$) and the *quasi-steady regime* ($t > 40N^{-1}$).

The vertical component $\langle w'^2_{3D}\rangle$ evolves somewhat differently (figure 10). Until $t = 25N^{-1}$, it strongly dominates, indicating that the three-dimensional perturbation added on θ essentially induces vertical motions in the early stages. Despite this, $\langle w'^2_{3D}\rangle$ starts growing at $t = 20N^{-1}$ at the same rate as $\langle u'^2_{3D}\rangle$ and $\langle v'^2_{3D}\rangle$. Between $t = 25N^{-1}$ and $t = 30N^{-1}$, however, $\langle w'^2_{3D}\rangle$ slightly decreases to the same amplitude as the other components. From $t = 30N^{-1}$, it grows again, but is now of the same order as $\langle u'^2_{3D}\rangle$ and $\langle v'^2_{3D}\rangle$. From then on, the three-dimensional motions do not deviate much from

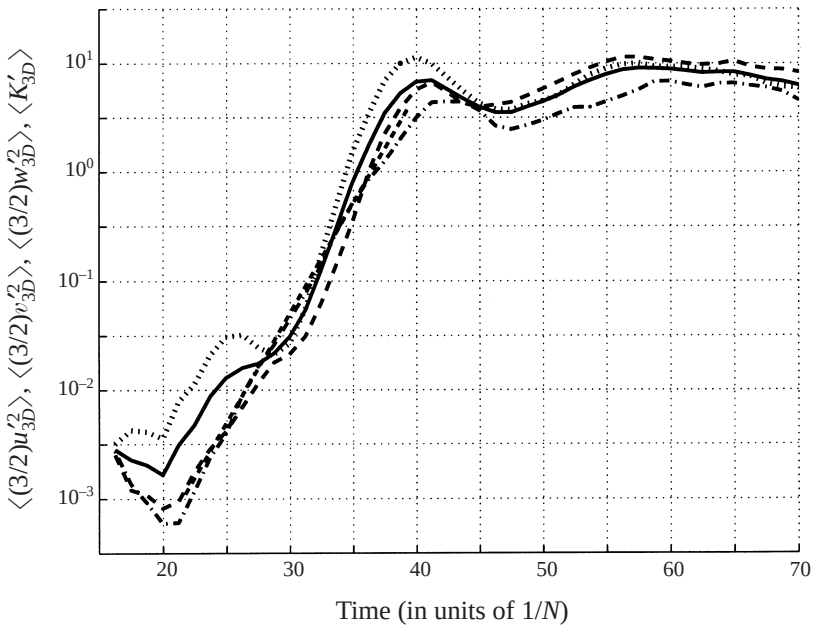

FIGURE 10. Evolution of the three-dimensional dynamics within the breaking region. (Simulation 4.) Dashed line: $(3/2)\langle u'^2_{3D}\rangle$. Dotted-dashed line: $(3/2)\langle v'^2_{3D}\rangle$. Dotted line: $(3/2)\langle w'^2_{3D}\rangle$. Solid line: K'_{3D}.

isotropy, as revealed by the rather good overlap of the curves $\frac{3}{2}\langle u'^2_{3D}\rangle$, $\frac{3}{2}\langle v'^2_{3D}\rangle$, $\frac{3}{2}\langle w'^2_{3D}\rangle$ and $K'_{3D} = \frac{1}{2}(\langle u'^2_{3D}\rangle + \langle v'^2_{3D}\rangle + \langle w'^2_{3D}\rangle)$ for $t > 30N^{-1}$.

4.2. *Vortex structures generated by the instability*

The three-dimensional vortex structures that are present within the breaking wave at the beginning of the quasi-steady regime are studied with vorticity fields. The vortices are well shaped by $t = 40N^{-1}$, corresponding to the local maximum peak of K'_{3D} in figure 10.

The streamlines at the very first times of the breaking have an 'S' shape in a longitudinal (x, z)-plane (figure 4, $t = 20N^{-1}$). This shape is induced by the two-dimensional overturning of the gravity wave. The two curves of the 'S' envelop regions with opposite y-vorticity, eventually leading to two counter-rotating vortices in the (x, z)-plane, as observed in both experiment and simulation in the early stage of the quasi-steady regime (figures 11*b* and 11*c*). However, these vortices are not two-dimensional. That is evident upon examination of the flow in the other planes. For example, the velocity-vector field in a frontal section (y, z) through the breaking region (figure 12) reveals counter-rotating vortices with a strong central downflow. Figure 13, showing a three-dimensional vorticity-modulus iso-surface at $t = 45N^{-1}$, suggests that these vortical stuctures have a toroidal geometry, in agreement with the experimental results of Eiff & Bonneton (2000). This geometry implies that the vorticity lines are closed in order to form an 'O'-shape. This can be verified in figure 14, showing the three components of vorticity in horizontal sections 1 and 2, indicated in figure 11(*a*) or 11(*b*), which intersect the cores of the two (x, z)-vortices of figure 11(*b*). The vorticity iso-contours in the upper section 1 (figure 14) show that the alternating positive and negative concentrations of strong streamwise vorticity (ω_x) are located downstream of both sides of a maximum of transversal vorticity

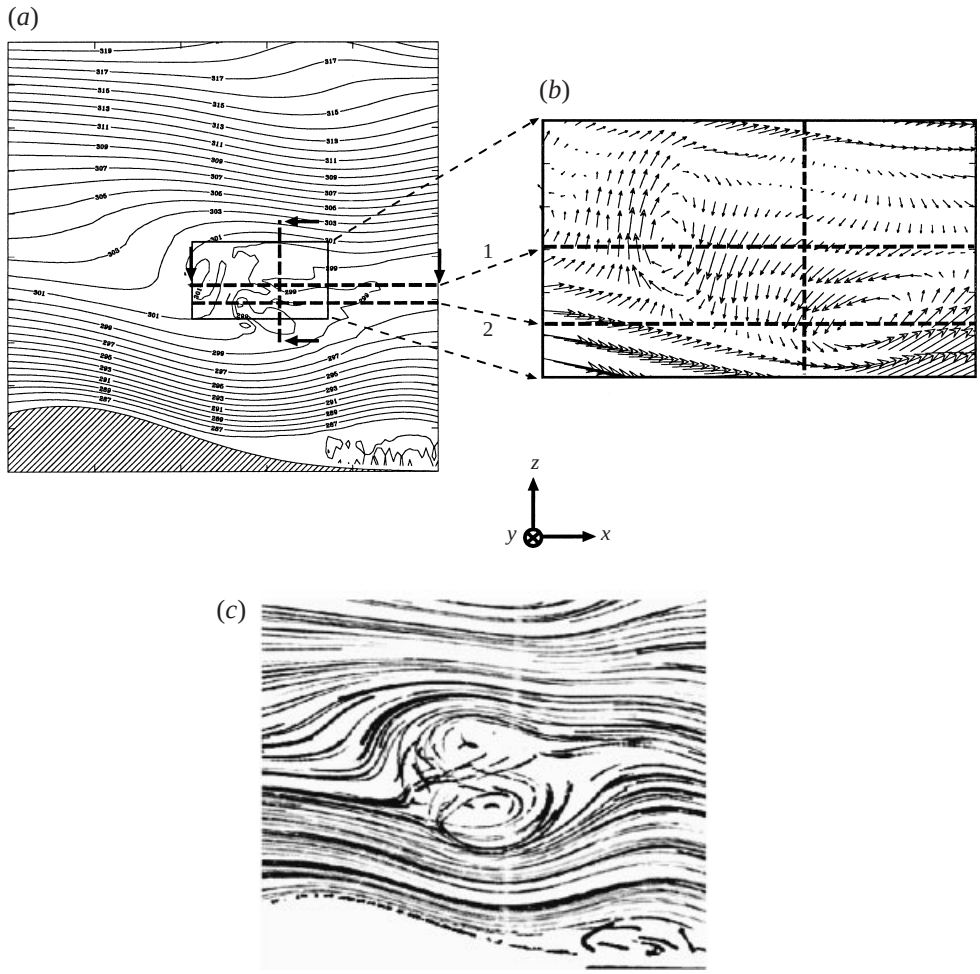

FIGURE 11. Details of the breaking dynamics in an (x, z)-plane. (*a*) Iso-θ contours at $t = 45N^{-1}$. The box delimits the enlarged view shown in (*b*), and the dashed lines indicate the location of the frontal (y, z) and horizontal (x, y) sections shown in figures 12 and 14 respectively. (*b*) $\boldsymbol{u}$ vector field at $t = 45N^{-1}$. ((*a*, *b*): Simulation 3.) (*c*) Experimental pathlines (integration time $= 10N^{-1}$) at $t = 50N^{-1}$.

(ω_y), implying that vorticity lines are locally in the shape of a 'U' (with the open end oriented downstream). In the lower section 2 (figure 14), the concentrations of ω_x are located upstream from a second but opposite maximum of ω_y, implying that vorticity lines are also in a 'U' shape but oriented in the opposite direction than above. Given the location of opposite concentrations of the vertical vorticity (ω_z) in the lower section (2), one can conclude that the two oppositely oriented 'U's actually form an 'O' shape, with the plane containing the 'O' sloping downwards for increasing x. This geometry contrasts with the streamwise vortices previously described in various cases of overturning waves (Fritts *et al.* 1994; Caulfield & Peltier 1994; Afanasyev & Peltier 1998). In these studies, vortices were depicted as elongated in the streamwise direction, without mention of possible up- and downstream closure of the vorticity lines. In our case, this particular vorticity-line closure is linked to the special morphology of the breaking region due to the presence of the trapped lee wave below. The latter

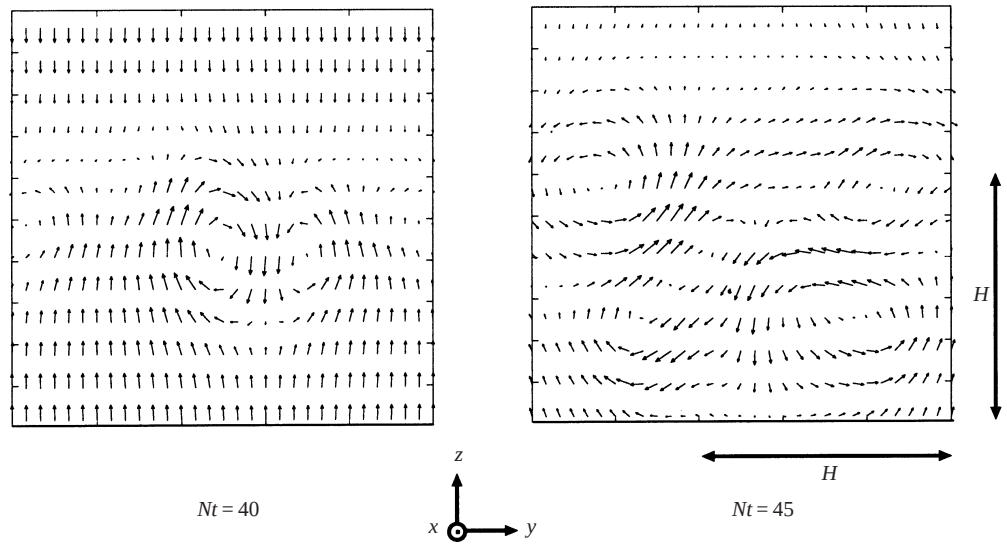

FIGURE 12. $\boldsymbol{u}$ vector field in the breaking region. The abscissa and the vertical dimension of this (y, z)-section are indicated with a vertical dashed line in figure 11(a). Longest arrows stand for about $0.6U_0$. Simulation 3.

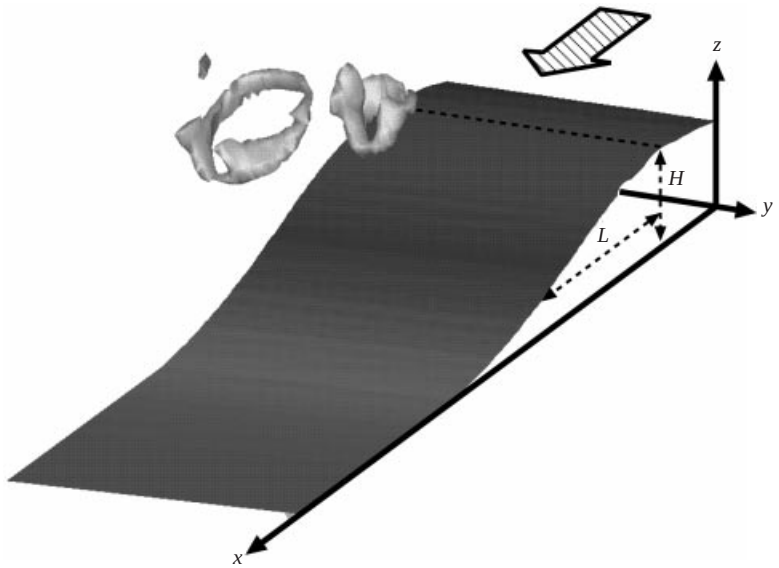

FIGURE 13. Vorticity-modulus iso-surface at $t = 45N^{-1}$ for the value $||\boldsymbol{\omega}|| = 2.8N$. The dashed line indicates the crest of the obstacle. Simulation 3.

tends to prevent the downstream propagation of the breaking wave, and the vorticies generated by the three-dimensional instability are confined upstream of the first peak of the trapped lee wave.

4.3. *Autocorrelation and spectral analysis*

The typical width of the vortices across the span of the flow can be evaluated by examining the autocorrelation function of the three-dimensional part of the velocity,

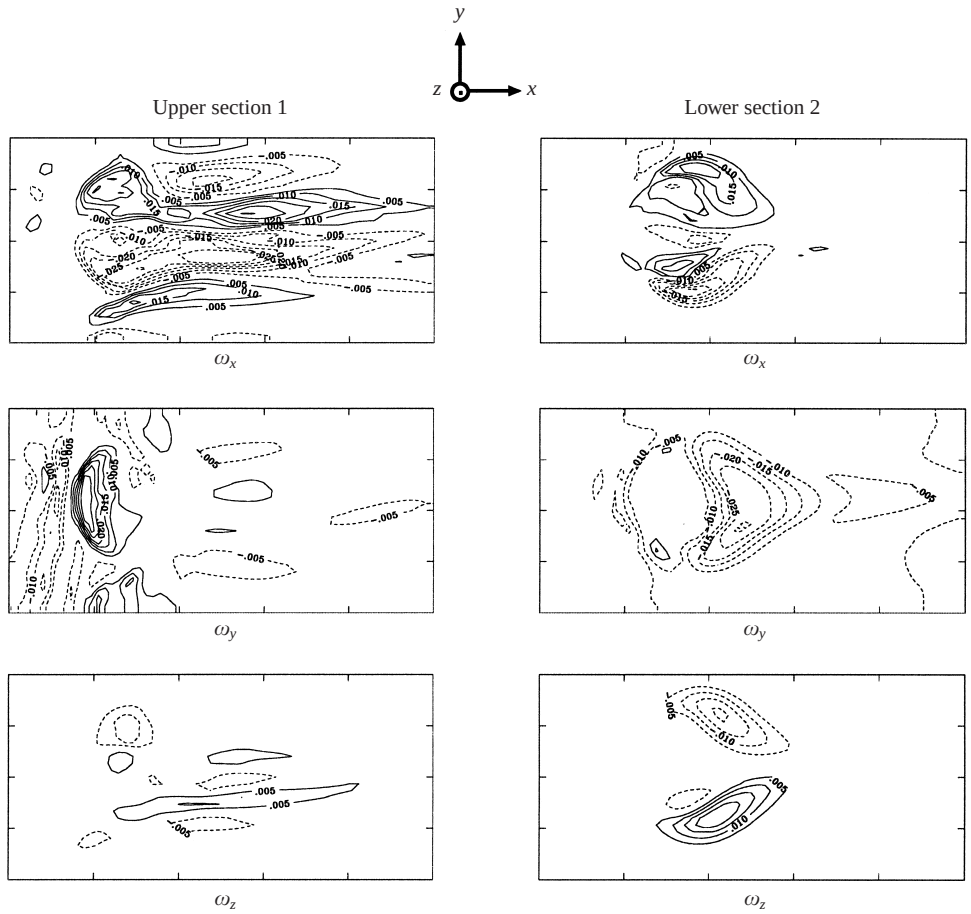

FIGURE 14. ω_x, ω_y and ω_z vorticity iso-contours (in units of $100N$) at $t = 45N^{-1}$ in the horizontal sections 1 and 2 indicated in figure 11. (Their altitudes and streamwise extent are given with the horizontal dashed lines in figure 11(*a*); their width is the same as in the frontal section of figure 12.) The vorticity structure corresponds to the left-hand torus in figure 13. Simulation 3.

$\boldsymbol{u}'_{3D}$, as a function of y given t, x and z. Omitting all explicit dependences except on y, it is defined by

$$\mathscr{A}(\delta y) = \frac{1}{C} \int_0^{L_y} \boldsymbol{u}'_{3D}(y) \cdot \boldsymbol{u}'_{3D}(y - \delta y)\, \mathrm{d}y,$$

where L_y is the width of the domain and $C = \int_0^{L_y} \boldsymbol{u}'^2_{3D}(y)\, \mathrm{d}y$. This autocorrelation function for the motions within the breaking region is plotted in figure 15 for $t = 40N^{-1}$ and $t = 50N^{-1}$. After a rapid decrease from one to zero, $\mathscr{A}(\delta y)$ oscillates in a manner characteristic of a quasi-periodic behaviour. Towards the end of the growth regime, at $t = 40N^{-1}$, the characteristic wavelength is about $1.2H$ (figure 15*a*). Since the vortices are toroidal, taking the form of counter-rotating pairs in the (y, z)-plane, the diameter, d, of a single vortex is about half the characteristic wavelength, i.e. $d \sim 0.6H$, corresponding to the size of the vortices shown in a (y, z)-plane in figure 12 at $t = 40N^{-1}$. One can verify that this dimension is close to the depth of the superadiabatic region at $t = 40N^{-1}$. For later times, the toroidal vortices evolve towards more complex vortex structures. The autocorelation at $t = 50N^{-1}$ (figure 15*b*)

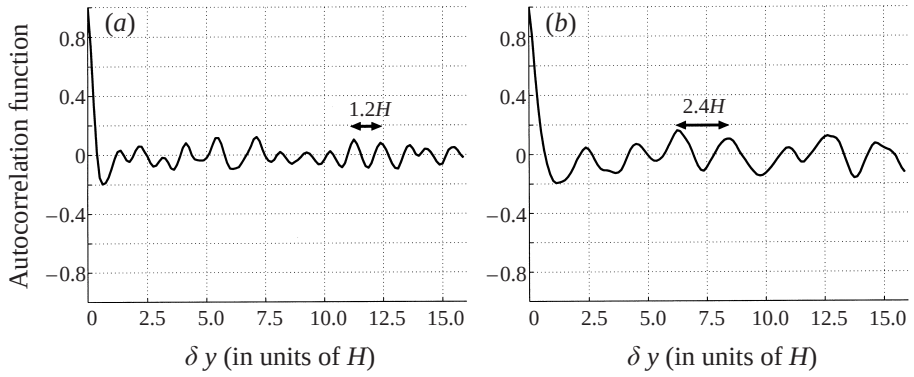

FIGURE 15. Autocorrelation function $\mathscr{A}(\delta y)$ of $\boldsymbol{u}'_{3D}(y)$ in the breaking region at (*a*) $t = 40N^{-1}$ and (*b*) $t = 50N^{-1}$. (Wide domain $L_y = 32H$, Simulation 4.)

now has a wavelength of about $2.4H$, and does not significantly evolve later. Thus the typical diameter of single vortices during the quasi-steady regime, $d \sim 1.2H$, is greater than at $t = 40N^{-1}$. It is slightly smaller than the depth of the mixed region at $t = 50N^{-1}$ (see table 2, D_{ml}) but remains of the same order of magnitude. (It should be remarked that the final quasi-steady mixed region is significantly deeper ($\sim 1.2H$) than the earlier superadiabatic region ($\sim 0.6H$).)

In order to analyse the spectral energy distribution of the three-dimensional motions, the kinetic energy (K) spectra in the cyclic y-direction are computed considering the components of $\boldsymbol{u}$ as functions of y. Spectra of $u(y)$, $v(y)$ and $w(y)$ (omitting the dependences on t, x and z) are computed using fast Fourier transforms (FFT) at five different locations (x_i, z_i) within the breaking region for $15N^{-1} < t < 80N^{-1}$. The final kinetic energy spectra presented in this paper are the mean over the five samples i in order to reduce statistical errors. In summary, they are defined by

$$K(n) = \tfrac{1}{2}\langle |\hat{\boldsymbol{u}}(x_i, z_i)(n)|^2 \rangle_i,$$

where $\hat{\boldsymbol{u}}(x_i, z_i)(n) = \mathrm{FFT}\,[\boldsymbol{u}(x_i, z_i)(y)]$, and the wavenumber $n = L_y/\lambda$ is the number of periods over the width of the domain.

The spectral distribution that we obtain with a wide domain simulation ($L_y = 32H$, simulation 4) is presented in figure 16. The spectrum at $t = 35N^{-1}$ reveals that the fastest growing modes are located at wavelengths between H and $2H$. Since one wavelength λ corresponds to a pair of periodically arranged counter-rotating vortices, each vortex is of diameter $d \sim \lambda/2$. Thus, the range of scales $H < \lambda < 2H$ corresponds to vortices of diameter $0.5H < d < H$. These scales still dominate at $t = 40N^{-1}$, but the energy maximum migrates towards larger scales until $t = 50N^{-1}$, as previously noted in the autocorrelation discussion. Thereafter the most energetic scales remain around $\lambda = 4H$ (the bandwidth of these energetic scales is rather large due to spatial and time averaging, but encompasses the characteristic frequencies of the autocorrelation in the y-direction). For the scales smaller than $2H$, the energy density decays according to a power law $K(n) \propto n^p$. For the current simulation 4 we can evaluate the exponent $p = -2.4 \pm 0.1$.

In the quasi-steady regime, the qualitative shape of the energy spectrum (prevalence of scales around $\lambda = 4H$ and decay at small scales according to a power law) is observed in all simulations. The sensitivity of the quantitative aspect of the decay is tested by comparing the spectra obtained with several domain widths and

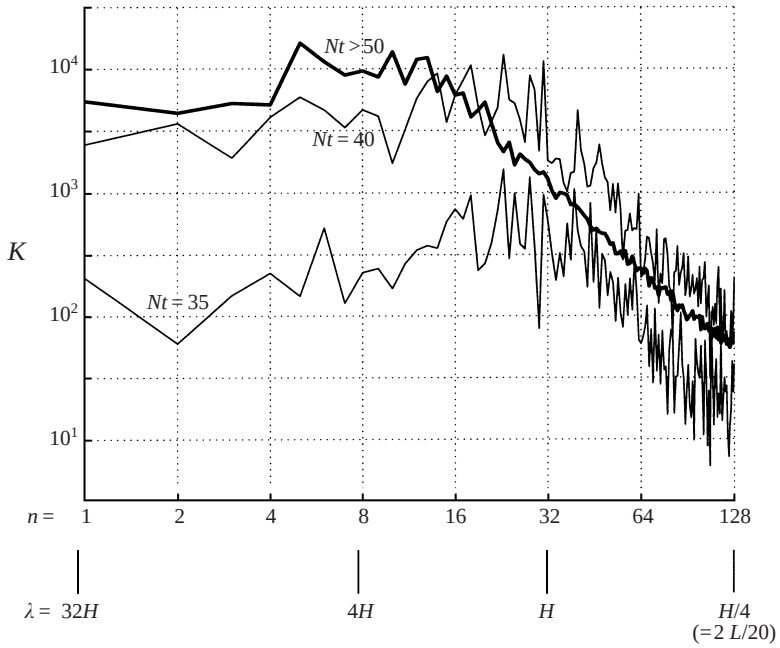

FIGURE 16. Kinetic energy spectrum, $K(n)$, of the three-dimensional motions within the wave-breaking region at $t = 35N^{-1}$ and $t = 40N^{-1}$ (thin curves), and for a temporal mean over $50N^{-1} < t < 80N^{-1}$ (thick curve). Simulation 4.

resolutions. Taking simulation 4 as the reference simulation, a finer simulation with an improvement by a factor two in resolution would lead to prohibitive numerical costs. Therefore, it is necessary to reduce the domain width before increasing the resolution. However, one must first verify that this reduced simulation gives the same spectra as the reference one with the same resolution. That was done in simulation 2 with a domain width reduced from $32H$ to $4H$. Figure 17 shows that the slope of the energetic decay at small scales does not depend on the domain width, i.e. the influence of scales larger than $4H$ on smaller scales is weak. The increased resolution (on the reduced domain) with a fine mesh of $\Delta x, y = L/40$ (twice as fine as in simulations 2 and 4) is performed in simulation 3. Within the observed fluctuations, all three spectra (which are shown superimposed in figure 17) overlap for $\lambda > H/2$ (or equivalently $\lambda > L/5$, i.e. twice the Nyquist scale of the coarse grid). For $\lambda < H/2$, however, there is too much energy in the coarse simulations (2 and 4), since there is no more transfer of energy towards smaller scales. Consequently, the overall slope of the energetic decay, evaluated between $H/4 < \lambda < 2H$, is stronger with the fine grid, about $p \simeq -3.5$. Thus, the behaviour of the very small scales is sensitive to the resolution, and a further improvement in resolution would be necessary to establish the convergence of p. However, the previous test validates the use of the mesh $\Delta x, y = L/20$ to simulate satisfactorily the most energetic processes, i.e. all scales greater than $H/2$. The energetic decay is also found to be more rapid than the $-\frac{5}{3}$ value of Kolmogorov's theory, implying a loss of kinetic energy. This could be due to viscous dissipation, inherent to the low Reynolds number studied, as well as loss against buoyancy forces, as suggested by Lumley (1964). In the case of nearly inertial turbulence in a stably stratified flow, Lumley derives a slope of -3.

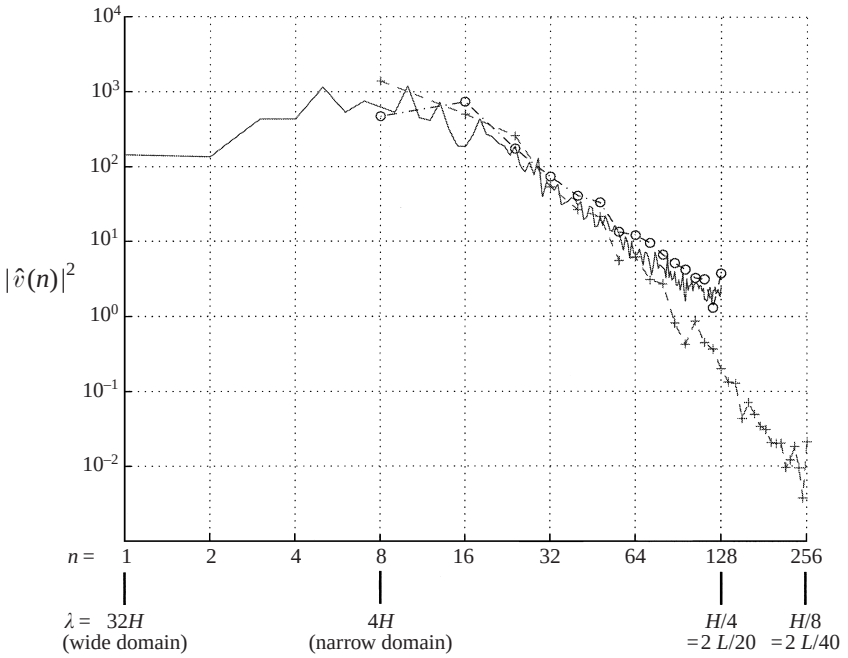

FIGURE 17. Comparison of spectra $|\hat{v}(n)|$. ——, Simulation 4 ($32H$ wide domain, $L/20$ mesh). ○—·—○, Simulation 2 ($4H$ narrow domain, $L/20$ mesh). +——+, Simulation 3 ($4H$ narrow domain, $L/40$ mesh). Each spectrum is a temporal mean from $t = 40N^{-1}$ to $50N^{-1}$. The wavenumber, n, is defined with respect to the wide domain: $n = 32H/\lambda$.

4.4. *Sensitivity to perturbation types*

In the previous subsections, the three-dimensional perturbation that was added on θ consisted of white noise, i.e. all scales in the flow were initially perturbed. We will now study the growth of the three-dimensional motions and their later evolution for two other types of three-dimensional perturbations: first, *harmonic disturbance*, where only one scale is excited, and second, *sidewalls*, where friction due to the sidewalls (as it exists in the experimental flow) is taken into account.

4.4.1. *Harmonic disturbance*

In simulation 5 ($32H$ wide domain), only one wavelength ($n_0 = 2$, i.e. $\lambda_0 = 16H$) was excited to create a harmonic disturbance. The initial three-dimensional circulations induced by the disturbance are counter-rotating circulations of width $8H$ (figure 18*a*), i.e. with an aspect ratio horizontal/vertical much greater than 1. Nevertheless, this wide stucture evolves into narrower vortices of aspect ratio of about 1 (figure 18*b*), as in the previous simulation (simulation 4) which was perturbed at all scales. This evolution can be explicitly shown by plotting the autocorrelation $\mathscr{A}(\delta y)$ at few successive times (figure 19*a*). In the early stages, the wide harmonic shape of the three-dimensional dynamics (induced by the disturbance) is reflected by a sinusoidal autocorrelation with the same period, but during the breaking, the autocorrelation function evolves toward a shape comparable to simulation 4 (figure 15), with a characteristic wavelength of the same order ($\lambda \sim 3H$ for simulation 5). This transition from large to small scales is well captured by the

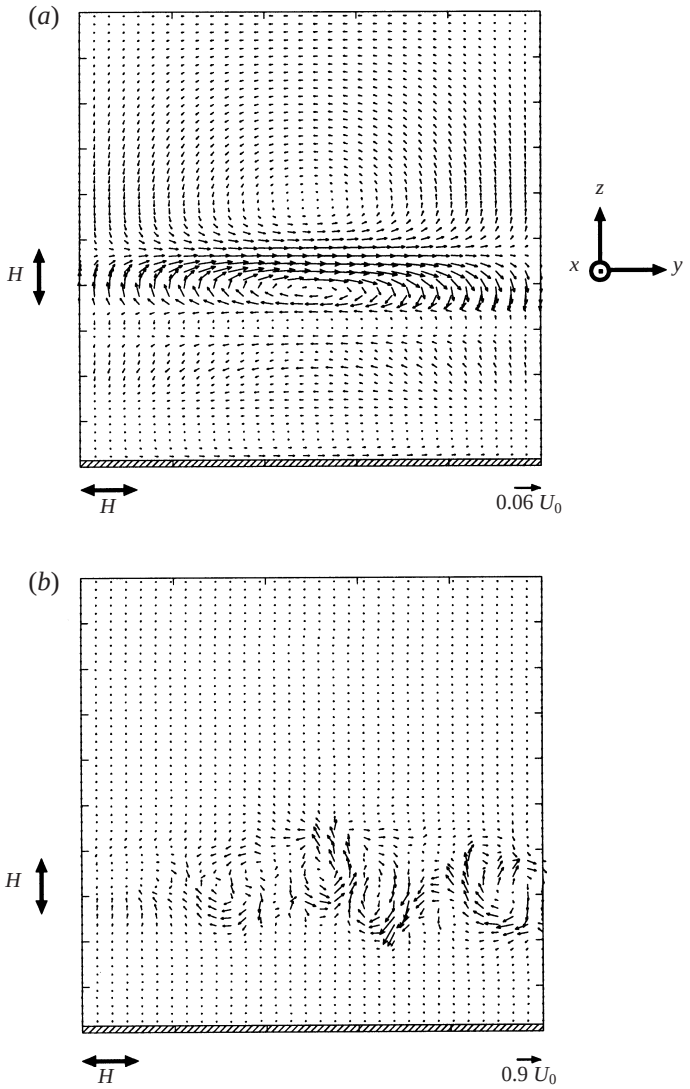

FIGURE 18. $\boldsymbol{u}'_{3D}$ vector field in a (y, z)-plane at (*a*) $t = 20N^{-1}$ and (*b*) $t = 60N^{-1}$. Since the motions in (*a*) are very weak, the vector scale is much larger than in (*b*). Simulation 5.

integral scale,

$$\Delta(t) = \int_0^{\delta y_0} \mathscr{A}(\delta y)\, \mathrm{d}\delta y,$$

where δy_0 is the first zero-crossing value. Figure 19(*b*) shows that the integral scale decays rather abruptly around $t = 35N^{-1}$, then remains steady after $t = 40N^{-1}$. Regarding the onset of the growth of the three-dimensional motions as was found in figure 10 ($t = 20N^{-1}$) the transition from wide circulations to narrower vortices is delayed by about $15N^{-1}$. In summary, the scales that were found to be the most energetic in the white noise case ($\lambda \sim 4H$) eventually dominate the flow even in the case of the harmonic perturbation with a longer wavelength ($\lambda = 16H$). However,

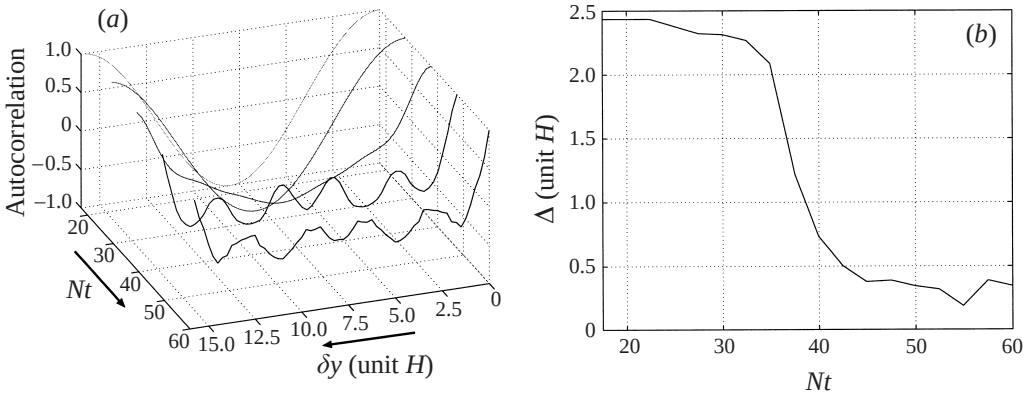

FIGURE 19. (*a*) Autocorrelation $\mathscr{A}(\delta y)$ profiles at $Nt = 17.5$, 27.5, 37.5, 47.5, and 60. (*b*) Integral scale $\Delta(t)$. Simulation 5.

these scales only dominate after a delay of $15N^{-1}$, implying a transfer of energy from $\lambda = 16H$ to $\lambda \sim 3H$ during this time interval.

A spectral analysis of simulation 5 shows that smaller and smaller scales are progressively excited by a cascade of energy towards the small scales (figure 20*a*). Furthermore, no energy is transferred in wavenumbers that do not belong to the harmonic series of the fundamental ($n_0 = 2$). Other simulations performed with harmonic perturbations of different wavelength (simulations 6,7,8) yield the same result: all the energy is transferred harmonically. This implies that the transfer of the energy towards small scales results from a process of nonlinear generation of harmonics. The phase shifts with respect to the 'fundamental' wavenumber $n_0 = 2$ (figure 20*b*) change from random values to coherent ones as soon as the corresponding harmonics are excited by the nonlinear cascade – as for instance for the wavenumber $n = 12$ in figure 20(*b*). At $t = 35N^{-1}$, it must be further remarked that the phase shifts are systematically $\pm 90°$ for the even harmonics (that is $n = 2n_0,\ 4n_0,\ 6n_0, \ldots$), and $0°$ or $\pm 180°$ for the odd ones (that is $n = 3n_0,\ 5n_0,\ 7n_0, \ldots$). Therefore, the acting nonlinear term in the cascade must be advection in the transversal direction y, i.e. $v\,\partial/\partial y$, since the product will add the wavenumbers, and the derivative will shift the phase by $\pm \pi/2$. This signature of transversal advection suggests that there is no strong interaction with the longitudinal (x, z)-dynamics during the breaking, implying that the three-dimensional motions in the transverse (y, z)-plane are rather independent from the two-dimensional wave dynamics (once the breaking conditions have been generated by the latter.) In their analytical stability studies of a stratified shear flow, Deardorff (1965) and Winters & Riley (1992) are led to the similar conclusion that the unstable dynamics of a spanwise-oriented disturbance is independant from the streamwise-oriented shear.

The above conclusion was found to be independent of the wavelength of the perturbations. Moreover, the evolution of the harmonic series for three different harmonic disturbances $n_0 = 1$, 2, and 4 (with $L_y = 4H$), given in simulations 6, 7, and 8 respectively (figure 21), shows that the evolution of a given wavenumber depends only on its rank in the harmonic series, and not on the fundamental wavenumber n_0. Hence the nonlinear coherent cascade process also seems to be independent of the scale of the perturbation, at least in this range of relatively small scales (since $n_0 = 1, 2, 4$ corresponds to $\lambda = 4H, 2H, H$ for $L_y = 4H$). The spectral energetic peaks

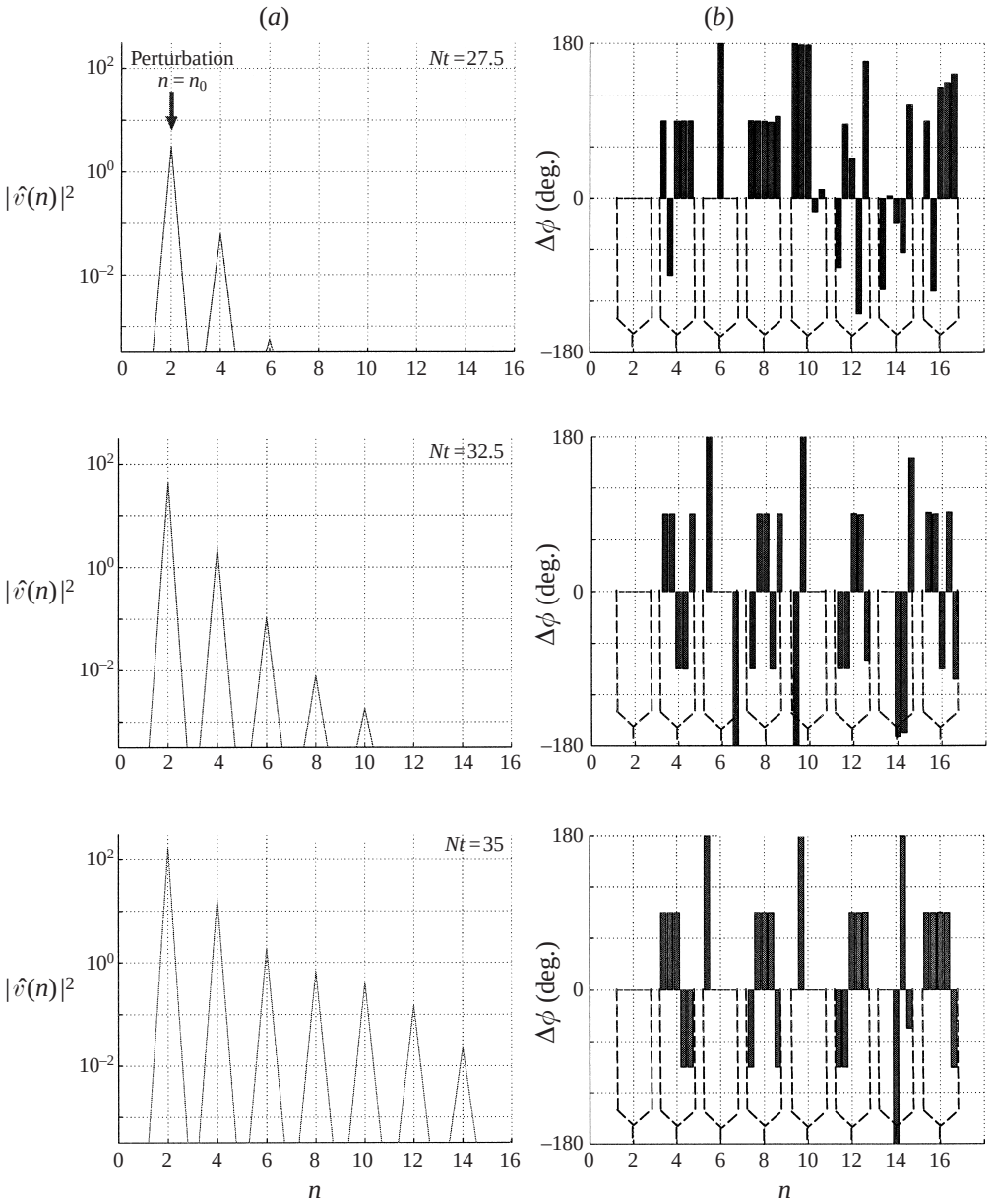

FIGURE 20. (*a*) Spectra $|\hat{v}(n)|$ at three times during the growth regime. (*b*) Corresponding phase shifts (even n only) with respect to the 'fundamental' wavenumber $n_0 = 2$; a group of five bars stands for the same wavenumber; each bar of the group stands for one of the five spectra defined in § 4.3. Simulation 5.

of all harmonic series reach saturation values such that their envelope has the same shape as the spectrum obtained by white-noise perturbation (figure 16).

4.4.2. *Sidewalls*

Unlike the first eight simulations, which used lateral cyclic boundary conditions, simulation 9 takes sidewalls with viscous friction into account, in direct correspon-

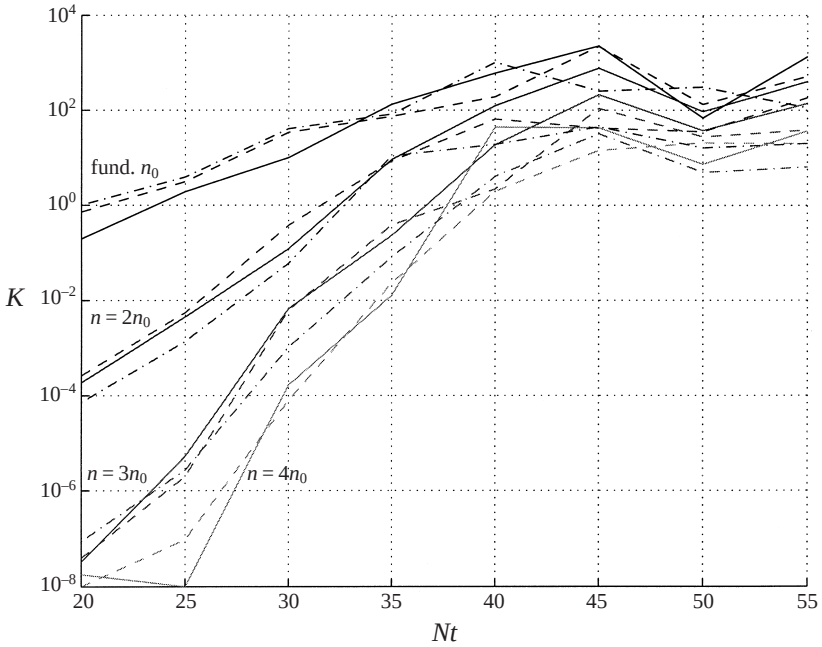

FIGURE 21. Temporal evolution of the first four harmonics in each of three simulations with harmonic disturbance, whose perturbation wavenumbers are $n_0 = 1$, solid line (Simulation 6), $n_0 = 2$, dashed line (Simulation 7), and $n_0 = 4$, dashed-dotted line (Simulation 8).

dance with the tank experiments. Consequently, the existence of a shear layer parallel to the sidewalls breaks the two-dimensional symmetry of the flow and no additional three-dimensional perturbation on the θ-field is needed. Sufficiently far from the walls, their presence does not have a great influence on the longitudinal (x, z) wave field in the early times of the breaking (figure 22*a*). Near the walls, the flow must approach $U_0\boldsymbol{e}_x$ since the walls are moving with the velocity $U_0\boldsymbol{e}_x$ in the obstacle frame, and the flow is accelerated in the longitudinal direction, as seen on figure 22(*b*). Thus, the initial three-dimensional motions acting to disturb the flow are strongest near the walls and the three-dimensional character of the breaking dynamics does not appear simultaneously across the whole width of the flow, but starts from the sides and gradually converges towards the central plane (figure 23). Near the centre, even at $t = 55N^{-1}$, no three-dimensional motions can be discerned in figure 23(*c*). In the vertical central plane however, breaking has already occurred.

At $t = 45N^{-1}$ (figure 24), the comparison of two longitudinal cross-sections, near the wall and near the central plane, indicates an important difference between the vortex patterns. Near the wall (figure 24*a*), two counter-rotating vortices are visible, corresponding to the presence of a three-dimensional toroidal vortex (figure 23*b*). Near the centre (figure 24*b*), only one vortex is observable. Since there are no significant three-dimensional motions in the central part of the channel over a width of about $12H$ (as one can see in figure 23*b*), there is actually a single quasi-two-dimensional vortex spanning transversally – which is expected in a strictly two-dimensional simulation.

Simulation 9 compares well with the experimental observations (Eiff & Bonneton 2000). Three-dimensional motions are first detected near the sidewalls; at the same time, a single quasi-two-dimensional roll, spanning transversally in the central part

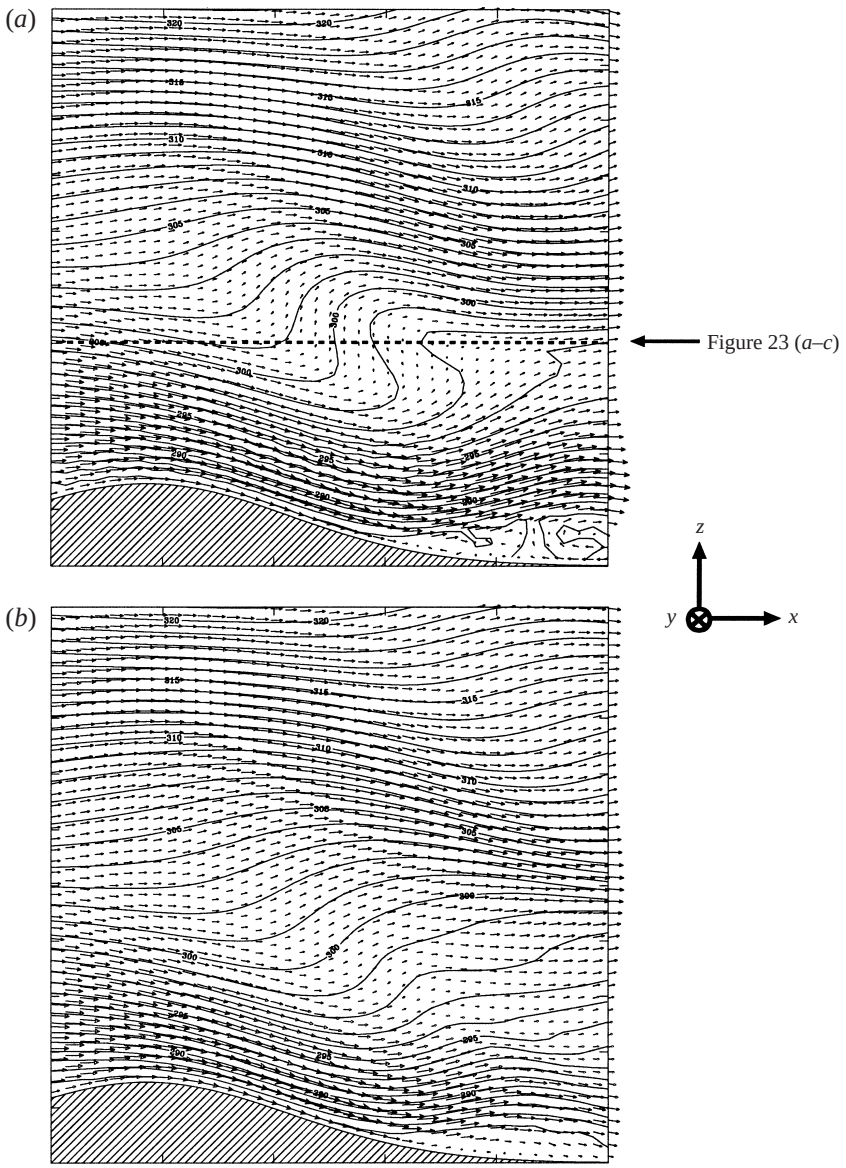

FIGURE 22. Flow at the beginning of the breaking at $t = 30N^{-1}$ (iso-θ contours in K and $\boldsymbol{u}$ velocity vectors; longest arrows stand for about $2.5\,U_0$). (*a*) Central vertical plane, (*b*) corresponds to the first grid point near the sidewall. See figure 23(*b*) for locations of planes (*a*) and (*b*). The dashed line in (*a*) shows the horizontal sections shown in figure 23. Simulation 9.

of the channel, forms prior the emergence of the toroidal vortices, corresponding to the temporary observation of the early stage of the unstable two-dimensional breaking.

However, the time needed to obtain significant three-dimensional motions across the whole width of the channel was observed to be shorter in the tank experiments than in simulation 9. Therefore, the influence of the walls in the hydraulic experiments may not be the only three-dimensional forcing from which the instability develops, and it is likely that the background 'noise' present in the tank has an additional influence.

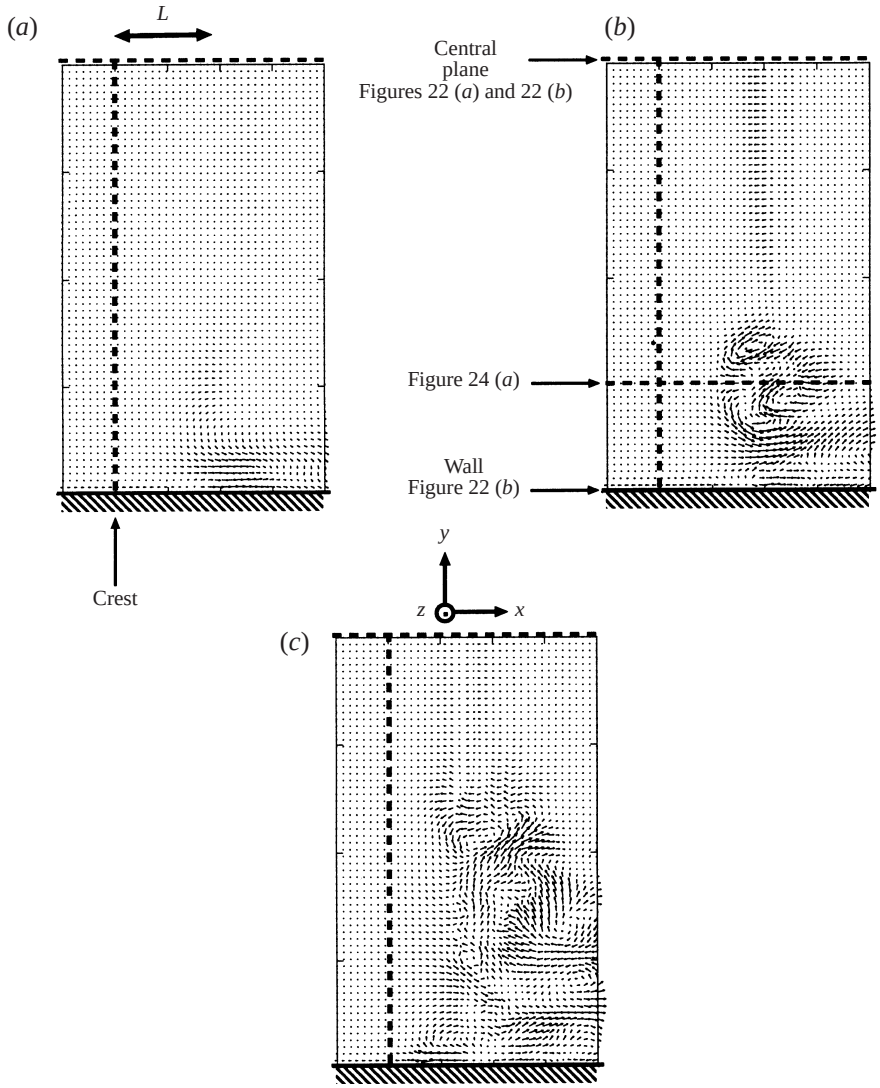

FIGURE 23. $\boldsymbol{u}'_{3D}$ vector field in the horizontal section at $z = 2.7H$ through the breaking region, indicated by a dashed line in figure 22(*a*). (*a*) $t = 35N^{-1}$, (*b*) $t = 45N^{-1}$, (*c*) $t = 55N^{-1}$. Simulation 9.

A simulation, which combines sidewalls with the white noise used for simulations 3 and 4 (with amplitude 0.3 K added to θ), would produce essentially the same results as those obtained with white noise alone, since the perturbations generated by the walls at the onset of the breaking ($t \sim 20N^{-1}$) would be negligible almost everywhere. We nevertheless expect a fine adjustment of the initial perturbation amplitude to lead to the same lifetime of the two-dimensional vortex as in the hydraulic experiments. We can conclude that the unstable two-dimensional breaking will be observed in the numerical as well as in the hydraulic experiments until three-dimensional motions dominate, and therefore the lifetime of the transient two-dimensional phase depends on the location and the amplitude of the initial perturbations from which the three-dimensional motions develop.

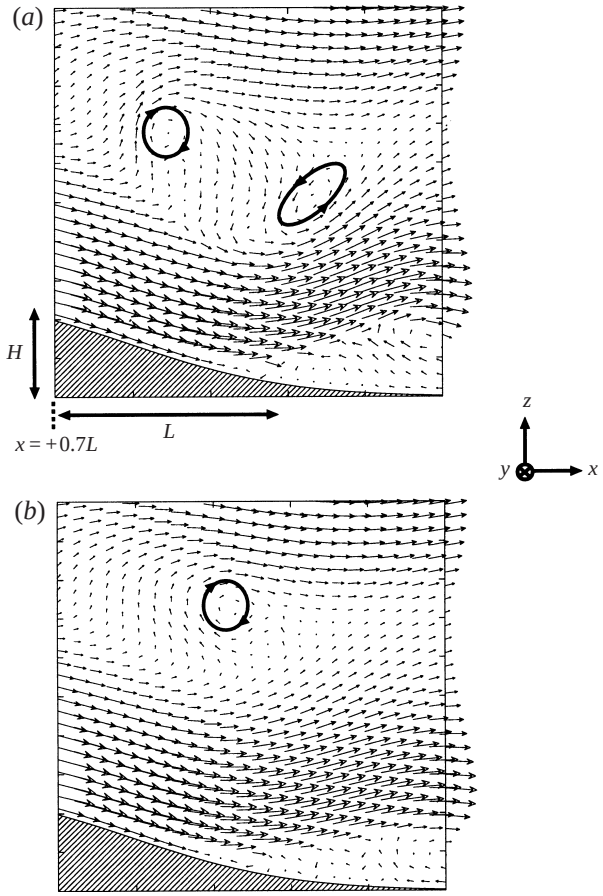

FIGURE 24. ***u*** velocity vectors at $t = 45N^{-1}$ (longest arrows stand for about $2.7\,U_0$). (*a*) Longitudinal plane $2.7H$ from the sidewall. (*b*) Central vertical plane. See figure 23(*b*) for locations of planes (*a*) and (*b*). Simulation 9.

5. Discussion

Part of our study concerns a direct comparison between the numerically simulated flow and the corresponding experimental flow. It was shown that the numerical atmospheric model *Meso-NH* can simulate an incompressible viscous stratified flow with a high degree of realism. The overall characteristics of the flow are captured with good quantitative agreement. The two-dimensional simulation confirms that the breaking wave enhances the strength of the low-altitude trapped lee wave at the expense of the high-altitude steepening wave. This point reinforces the earlier idea that the mixed region due to the breaking acts as a reflector of energy and traps it in the lower levels (Peltier & Clark 1979, 1983), at least for this range of wavelengths. We also established that the trapped lee wave only appears in the presence of ground friction which induces a separation of the laminar boundary layer on the lee slope of the mountain. The trapped lee wave considerably influences the breaking region above, preventing the latter from propagating downstream (as it does under free-slip conditions at the ground). Instead, the breaking region consists of cores of mixed fluid located above the troughs of the trapped lee wave.

Three-dimensional simulations were used to investigate the three-dimensional

nature of the breaking. Before the breaking, the wave dynamics remain two-dimensional, but the overturning of the iso-θ contours leads to a region of statically unstable fluid. This two-dimensional configuration becomes unstable with respect to small three-dimensional disturbances, and the velocity characteristic of the three-dimensional motions grows exponentially at a rate of about $5N^{-1}$. The motions that develop in the transverse plane during the growth phase of the instability are organized in the form of counter-rotating pairs of vortices with strong adjacent up- and downflows. However, they do not correspond to the streamwise elongated alternating vortices often depicted in the literature on overturning internal waves, but rather to the toroidal vortices observed in the experiments by Eiff & Bonneton (1998, 2000). This particular geometry is linked to the presence of the trapped lee wave below, which prevents the streamwise elongation of the vortices. Instead, the vorticity lines are closed approximately above the first peak of the trapped lee wave. These vortices have transverse and vertical dimensions of the same order, i.e. a diameter $0.5H < d < 1H$, which corresponds to the depth of the superadiabatic layer during the growth phase of the instability. Fritts *et al.* (1994) made the same observation for the transverse geometry of the streamwise elongated vortices, and Klaasen & Peltier (1985) also found with a linear perturbation method that the most unstable mode has a transverse wavelength close to the depth of the superadiabatic region.

In the case of white-noise disturbance, spectral analysis of the kinetic energy during the growth regime showed that the fastest growing modes correspond to the typical wavelength of the toroidal vortices. However, because of strong nonlinear interaction between scales, the growth rate of each mode depends on the spectral type of the initial three-dimensional disturbance. In the case of a harmonic disturbance, there is a coherent cascade of energy towards the small scales via a generation of harmonics due to the nonlinear term of transverse advection $v\,\partial/\partial y$.

The geometry in the (y, z)-plane of the counter-rotating pairs of vortices is typical of the motions that occur in the early stages of overturning internal waves engendered by the growth of transverse instabilities. Klaassen & Peltier (1985) and Winters & Riley (1992) showed the convective nature of such instabilities with linear perturbation methods. We may provide a complementary argument in favour of that conclusion in the nonlinear stage of the instability: the transverse advection term $v\,\partial/\partial y$ was shown to dominate the other nonlinear terms governing the dynamics in the (y, z)-plane. This indicates that there is no strong coupling, in the early stages of the breaking, between the transverse and the longitudinal dynamics. Therefore, the transverse motions do not appear to derive their energy from longitudinal shear, but rather from potential energy in the convectively unstable region.

After the growth phase, the three-dimensional motions within the breaking region reach a quasi-steady regime, and the toroidal vortices degenerate towards more complex motions. Vortices of diameter $1H < d < 2H$ nevertheless dominate. This size is comparable to the value $d \sim 1.5H$ observed in the tank experiments, and is also of the order of the depth of the mixed region. During the quasi-steady regime, the size of these vortices does not depend on the type of the initial perturbation.

In our case, no underlying shear is present in our basic state to maintain the turbulence in the breaking region. A zone of possible shear production of turbulence (i.e. in terms of the local Richardson number, $0 < Ri < 0.25$)† is generated and maintained by the wave dynamics at the bottom edge of the mixed region. In the

† We use the experimental criterion $0 < Ri < Ri_c = 0.25$, but it strictly stands for high Reynolds number parallel shear flows. The critical value is probably closer to zero for $Re = 200$.

case of orographic wave breaking with no underlying shear studied by Afanasyev & Peltier (1998), Kelvin–Helmholtz billows develop in this zone, and contribute in an important way to sustaining the turbulent motions in the entire mixed region. Evidence of Kelvin–Helmholtz instability was neither observed in the tank experiments for $Re = 200$ nor in our simulations. Thus, the question of how the turbulence is maintained in our case still remains.

Two-dimensional wave breaking appears to be an unrealistic solution of the physical problem investigated here. The two-dimensional simulation (simulation 1) showed an intermittent evolution over long time scales for the mixed region that is not consistent with the experimental results. Andreassen *et al.* (1994) have already stressed that two-dimensional simulations of breaking internal waves lead to physically wrong results. In the early stage of the breaking, a transient quasi-two-dimensional roll is nevertheless observed in the experiment (Eiff & Bonneton 2000), corresponding to an unstable two-dimensional solution. However, we have shown that this observation depends on the location and the amplitude of the three-dimensional perturbation from which the instability develops.

This numerical study was performed with a low Reynolds number ($Re = 200$) linked to the experimental conditions. The follow-up of these parallel experimental and numerical studies will be with more atmospherically realistic Reynolds number values around 10 000. Experiments in a large channel (1 m $\times$ 3 m $\times$ 20 m) will enable measurements of turbulence in the breaking region. They will be used to study the structure of the turbulence generated by the wave breaking, and also to further validate the *Meso-NH* model. It will be particularly interesting to test the relevance of various sub-grid turbulence schemes in such conditions. After validation, numerical simulations at still higher Reynolds will allow us to study to what extent hydraulic experiments can reproduce the dynamics of the atmosphere ($Re = \infty$) past a range of mountains.

This work was financially supported by the CNRS program PATOM. We are grateful to Philippe Bonneton (University Bordeaux I, France) for helpful discussions.

REFERENCES

Afanasyev, Y. & Peltier, W. 1998 The three-dimensionalization of stratified flow over two-dimensional topography. *J. Atmos. Sci.* **55**, 19–39.

Andreassen, O., Wasberg, C., Fritts, D. & Isler, J. 1994 Gravity wave breaking in two and three dimensions: 1. Model description and comparison of two-dimensional evolutions. *J. Geophys. Res.* **99**, 8095–8108.

Arakawa, A. & Mesinger, F. 1976 Numerical methods used in atmospheric models. *GARP Tech. Rep.* **17**.

Asselin, R. A. 1972 Frequency filter for time integrations. *Mon. Wea. Rev.* **100**, 487–490.

Baines, P. G. 1995 *Topographic Effects in Stratified Flows*. Cambridge University Press.

Belcher, S. & Hunt, J. 1998 Turbulent flows over hills and waves. *Ann. Rev. Fluid Mech.* **30**, 507–538.

Bonneton, P., Auban, O. & Perrier, M. 1999 Experiments on two-dimensional lee-wave breaking in stratified flow. IMA *Conf. Proc. on Mixing and Dispersion in Stably Stratified Flows*, vol. 68, pp. 505–520. Clarendon.

Carpenter, K. M. 1982 Note on the paper "Radiation conditions for lateral boundaries of limited-area numerical models". *Q. J. R. Met. Soc.* **108**, 717–719.

Castro, I. P. & Snyder, W. H. 1993 Experiments on wave breaking in stratified flow over obstacles. *J. Fluid Mech.* **255**, 195–211.

Caulfield, C. & Peltier, W. 1994 Three dimensionalization of the stratified mixing layer. *Phys. Fluids* **6**, 3803–3805.

Clark, T. L. 1977 A small scale dynamical model using a terrain-following coordinate transformation. *J. Comput. Phys.* **24**, 186–215.

Clark, T. L. & Farley, R. D. 1984 Severe downslope circulations in two and three spatial dimensions using anelastic interactive grid nesting: a possible mechanism for gustiness. *J. Atmos. Sci.* **41**, 329–350.

Clark, T. L. & Peltier, W. R. 1977 On the evolution and stability of finite amplitude mountain waves. *J. Atmos. Sci.* **34**, 1715–1730.

Clark, T. L. & Peltier, W. R. 1984 Critical level reflection and the resonant growth of nonlinear mountain waves. *J. Atmos. Sci.* **41**, 3122–3134.

Davies, H. C. 1976 A lateral boundary formulation for multi-level prediction models. *Q. J. R. Met. Soc.* **102**, 405–418.

Deardorff, J. 1965 Gravitational instability between horizontal plates with shear. *Phys. Fluids* **8**, 1027–1030.

Dörnbrack, A. 1998 Turbulent mixing by breaking gravity waves. *J. Fluid Mech.* **375**, 113–141.

Durran, D. R. 1990 Mountain waves and downslope winds. *Atmospheric Processes over Complex Terrain* (ed. W. Blumen), pp. 59–81. *Am. Met. Soc.*

Eiff, O. & Bonneton, P. 1998 Vortex structure of a breaking wave in stratified flow over an obstacle. In *Advances in Turbulence VII* (ed. U. Frisch), pp. 471–474. Kluwer.

Eiff, O. & Bonneton, P. 2000 Lee-wave breaking over obstacles in stratified flow. *Phys. Fluids* to appear.

Fritts, D., Isler, J. & Andreassen, O. 1994 Gravity wave breaking in two and three dimensions: 2. Three-dimensional evolution and instability structure. *J. Geophys. Res.* **99**, 8109–8123.

Gal-Chen, T. & Sommerville, R. 1975 On the use of a coordinate transformation for the solution of the Navier–Stokes equations. *J. Comput. Phys.* **17**, 209–228.

Isler, J., Fritts, D., Andreassen, O. & Wasberg, C. 1994 Gravity wave breaking in two and three dimensions: 3. Vortex breakdown and transition to isotropy. *J. Geophys. Res.* **99**, 8125–8137.

Klaasen, G. & Peltier, W. 1985 The onset of turbulence in finite-amplitude Kelvin–Helmholtz billows. *J. Fluid Mech.* **155**, 1–35.

Klaasen, G. & Peltier, W. 1991 The influence of stratification on secondary instability in free shear layers. *J. Fluid Mech.* **227**, 71–106.

Lafore, J., Stein, J., Asencio, N., Bougeault, P., Ducrocq, V., Duron, J., Fischer, C., Héreil, P., Mascart, P., Redelsperger, J., Richard, E. & Vilà-Guerau de Arellano, J. 1997 The Meso-NH atmospheric simulation system. Part I: Adiabatic formulation and control simulations. *Annales Geophysicae* **16**, 90–109.

Landau, L. & Lifschitz, E. 1959 *Fluid Mechanics*. Pergamon.

Laprise, R. & Peltier, W. R. 1989 On the structural characteristics of steady finite-amplitude mountain waves over bell-shaped topography. *J. Atmos. Sci.* **46**, 586–595.

Lipps, F. B. & Hemler, R. S. 1982 A scale analysis of deep moist convection and some related numerical calculations. *J. Atmos. Sci.* **39**, 2192–2210.

Long, R. R. 1954 Some aspects of the flow of stratified fluids. Part II: Experiments with a two fluids system. *Tellus* **6**, 97–115.

Lumley, J. 1964 The spectrum of nearly inertial turbulence in a stably stratified fluid. *J. Atmos. Sci.* **21**, 99–102.

Peltier, W. & Clark, T. 1979 The evolution and stability of finite amplitude mountain waves. Part II: Surface wave drag and severe downlope winds. *J. Atmos. Sci.* **36**, 1498–1529.

Peltier, W. & Clark, T. 1983 Nonlinear mountain waves in two and three spatial dimensions. *Q. J. R. Met. Soc.* **109**, 527–548.

Queney, P. 1936 Recherches relatives à l'influence du relief sur les éléments météorologiques (1). *La Météorologie*, July–Aug. pp. 334–353.

Queney, P. 1948 The problem of air flow over mountains: a summary of theoretical studies. *Bull. Am. Met. Soc.* **29**, 16–26.

Richard, E., Mascart, P. & Nickerson, E. C. 1989 On the role of surface friction in downslope windstorms. *J. Appl. Met.* **28**, 241–251.

Rottman, J. W. & Smith, R. B. 1989 A laboratory model of severe downslope winds. *Tellus* **41A**, 401–415.

Schlichting, H. 1979 *Boundary Layer Theory*, 7th Edn. McGraw-Hill.

Scinocca, J. & Peltier, W. 1993 The instability of long's stationary solution and the evolution

toward severe downslope windstrom flow, part i: Nested grid numerical simulation. *J. Atmos. Sci.* 50, 2245–2263.

Scinocca, J. & Shepherd, T. 1992 Nonlinear wave activity conservatin laws and hamiltonian structure for the two-dimensional anelastic equations. *J. Atmos. Sci.* **49**, 5–27.

Scorer, R. S. 1949 Theory of waves in the lee of mountains. *Q. J. R. Met. Soc.* **75**, 41–56.

Smith, R. B. 1985 On servere downslope winds. *J. Atmos. Sci.* **42**, 2597–2603.

Smith, R. B. 1989 Hydrostatic airflow over mountains. *Adv. Geophys.* **31**, 1–41.

Stein, J. 1992 Investigation of the regime diagram of hydrostatic flow over a mountain with a primitive equation model. Part I: two dimensional flows. *Mon. Wea. Rev.* **120**, 2962–2976.

Thorpe, S. 1985 Laboratory observations of secondary structures in Kelvin–Helmholtz billows and consequences for ocean mixing. *Geophys. Astrophys. Fluid Dyn.* **34**, 175.

Viviand, H. 1974 Formes conservatives des équations de la dynamique des gaz. *La Recherche Aérospatiale* **1974-1**, 65–66.

Winters, K. & D'Asaro, E. 1994 Three dimensional wave instability near a critical level. *J. Fluid Mech.* **272**, 255-284.

Winters, K. & Riley, J. 1992 Instability of internal waves near a critical level. *Dyn. Atmos. Oceans* **16**, 249–278.